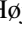




Demonstration of metaplectic geometrical optics for reduced modeling of plasma wavesRune Højlund Marholt ^{1,*}, Mads Givskov Senstius ² and Stefan Kragh Nielsen ¹¹*Section for Plasma Physics and Fusion Energy, Department of Physics, Technical University of Denmark, DK-2800 Kgs. Lyngby, Denmark*²*Rudolf Peierls Centre for Theoretical Physics, University of Oxford, Oxford OX1 3NP, United Kingdom*

(Received 8 February 2024; accepted 9 July 2024; published 27 August 2024)

The Wentzel, Kramers, and Brillouin (WKB) approximation of geometrical optics is widely used in plasma physics, quantum mechanics, and reduced wave modeling, in general. However, it is well-known that the approximation breaks down at focal and turning points. In this paper, we present an unsupervised numerical implementation of the recently developed metaplectic geometrical optics framework, which extends the applicability of geometrical optics beyond the limitations of WKB, such that the wave field remains finite at caustics. The implementation is in 1D and uses a combination of Gauss-Freud quadrature and barycentric rational function inter- and extrapolation to perform an inverse metaplectic transform numerically. The capabilities of the numerical implementation are demonstrated on Airy's and Weber's equations, which both have exact solutions to compare with. Finally, the implementation is applied to the plasma physics problem of linear conversion of X mode to electron Bernstein waves at the upper hybrid layer and a comparison is made with results from fully kinetic particle-in-cell simulations. In all three applications, we find good agreement between the exact results and a reduced wave modeling paradigm of metaplectic geometrical optics.

DOI: [10.1103/PhysRevE.110.025208](https://doi.org/10.1103/PhysRevE.110.025208)**I. INTRODUCTION**

Ray-tracing methods based on geometrical optics (GO) are widely used for reduced wave modeling, in general, and in fusion plasmas, in particular (Refs. [1,2]). Within plasma physics, examples of applications include various beam-based diagnostics (Refs. [3,4]), electron cyclotron resonance heating and current drive (Ref. [5]), as well as suppression of instabilities (Ref. [6]). Unfortunately, the underlying eikonal Wentzel, Kramers, and Brillouin (WKB) approximation behind GO theory typically breaks down at reflection points and focal points. Such critical points are, in general, called caustics. Caustics are common in plasma physics and they often occur in critical regions for mode coupling, which makes them essential for various diagnostics and advanced mode coupling schemes, Refs. [7,8]. Waves typically experience a natural amplification or swelling near caustics which means that several nonlinear effects can become particularly important [9,10]. Calculating the impact of these nonlinear wave effects relies crucially on the amplitude of the wave field at the caustics, Ref. [11]. However, the breakdown of the eikonal approximation means that the wave amplitude obtained from GO erroneously diverges. For this reason, many wave phenomena are challenging to model properly using reduced models based on GO and one must instead resort to computationally expensive full-wave codes [12,13].

In the recent works of Refs. [14–19], Lopez and coworkers proposed a method known as metaplectic geometrical optics (MGO) for reinstating the validity of GO in caustic regions. MGO takes a geometrical solution strategy by recognizing that the singularities in GO arise whenever the projection

of a ray trajectory from phase space to position space is singular. This is not unlike the widely used Maslov method (Refs. [20,21]) which works by evolving the wave field in Fourier space which effectively corresponds to representing the ray trajectory in a rotated phase space, thereby eliminating some projection singularities. The MGO method takes the Maslov method a step further by continuously applying a metaplectic transform, which corresponds to a continuous rotation of phase space in a manner such that the projection of the ray trajectory to the rotated position space is always well-defined locally. In Refs. [14–19], Lopez and coworkers developed and demonstrated the MGO method analytically on a few well-chosen key examples, but the method remained to be implemented in a fully automated numerical code. In this paper, we have developed an automated 1D implementation of the MGO framework which differs from previous semi-analytical demonstrations of MGO by calculating all quantities fully numerically, including the inverse metaplectic transform which we shall return to in Sec. III. The code is openly accessible on a repository on GitHub, Ref. [22]. As we shall explain in Sec. IV D, a particular challenge in evaluating the inverse metaplectic transform is how to analytically continue a numerical field from the real to the complex domain. This subproblem can be accomplished using barycentric rational interpolation. We demonstrate the results of this proposed method in Sec. V.

In the following, we first present the main ideas and analytical foundations of GO and MGO in Secs. II and III. In Sec. IV, we then describe the numerical details of our implementation of MGO, for which evaluating the inverse metaplectic transform is the main challenge and is achieved with barycentric rational interpolation and Gauss-Freud quadrature. In Secs. V A and V B, we present results of applying the method to Airy's equation and Weber's equation, which are fundamental wave physics problems with known

*Contact author: rjoho@dtu.dk

exact analytical solutions as well as analytical MGO solutions. Finally, in Sec. VC we apply the MGO code to a caustic occurring in plasma physics when an electromagnetic X mode couples to electron Bernstein waves (EBWs) at the upper hybrid layer to showcase a less idealized application. The MGO results are compared to results from fully kinetic particle-in-cell (PIC) simulations.

II. GEOMETRICAL OPTICS

In this paper, we consider time-stationary scalar linear wave equations of the integrodifferential form

$$\int d\mathbf{x}' D(\mathbf{x}, \mathbf{x}') \psi(\mathbf{x}') = 0, \quad (1)$$

where \mathbf{x} is the position coordinate, $D(\mathbf{x}, \mathbf{x}')$ is the wave operator kernel, and $\psi(\mathbf{x})$ is some wave field such as a scalar electric field or a quantum mechanical wave function. To the best of our knowledge, the MGO theory has not yet been generalized to time-dependent, vector-valued waves, but this is not an intrinsic limitation to the theory. Also note that our first iteration of a numerical implementation is only in 1D, i.e., $\mathbf{x} = x \in \mathbb{R}$. However, we use vector notation in Secs. II and III, since Refs. [14–19] have already derived the MGO theory in multiple dimensions.

The full integrodifferential wave equation in Eq. (1) can be simplified by assuming the wave field to be of the eikonal form:

$$\psi(\mathbf{x}) = \phi(\mathbf{x}) e^{i\theta(\mathbf{x})}. \quad (2)$$

Here $\phi(\mathbf{x})$ is the envelope and $\theta(\mathbf{x})$ is the phase. Within the theory of GO, the envelope $\phi(\mathbf{x})$ is assumed to vary much more slowly compared to the phase such that high order derivatives of $\phi(\mathbf{x})$ can be neglected. This can also be expressed in the eikonal parameter which is assumed small,

$$\epsilon = \frac{1}{kL} \ll 1, \quad (3)$$

where $k \sim |\partial_{\mathbf{x}}\theta|$ is the characteristic scale of variation of the phase and $1/L \sim |\partial_{\mathbf{x}}\phi|$ is the envelope variation scale. The eikonal approximation of Eq. (3) is also known as the WKB or the Liouville and Green approximation (Ref. [1], p. 22) and a medium satisfying the eikonal criterion is said to be weakly inhomogenous (Ref. [23]). To first order in ϵ , the full wave equation of (1) can be simplified to the GO equations (Refs. [1,24]):

$$\mathcal{D}[\mathbf{x}, \mathbf{k}(\mathbf{x})] = 0, \quad (4a)$$

$$\mathbf{v}(\mathbf{x}) \cdot \partial_{\mathbf{x}}\phi(\mathbf{x}) + \frac{1}{2}[\partial_{\mathbf{x}} \cdot \mathbf{v}(\mathbf{x})]\phi(\mathbf{x}) = 0, \quad (4b)$$

where $\mathbf{k}(\mathbf{x})$ and $\mathbf{v}(\mathbf{x})$ are, respectively, the local wave number and group velocity defined by

$$\mathbf{k}(\mathbf{x}) := \partial_{\mathbf{x}}\theta(\mathbf{x}), \quad \mathbf{v}(\mathbf{x}) := -\partial_{\mathbf{k}}\mathcal{D}(\mathbf{x}, \mathbf{k})|_{\mathbf{k}=\mathbf{k}(\mathbf{x})}. \quad (5)$$

Here $\mathcal{D}(\mathbf{z})$ is the dispersion symbol which is a function of phase space coordinates $\mathbf{z} = (\mathbf{x}, \mathbf{k})^T$ and is assumed to be real implying that we neglect dissipation. To be clear: \mathbf{k} is generally any wave vector, whereas the *local wave vector* $\mathbf{k}(\mathbf{x})$ is a specific function of \mathbf{x} for which (4a) is satisfied. There are multiple paths for deriving the GO equations, Eq. (4). A modern approach found in, e.g., Refs. [1,24] is to use Weyl symbol calculus, which makes it possible to approximate the

wave equation's differential operator by Taylor expanding its Weyl symbol in the eikonal parameter, Eq. (3). In this approach, $\mathcal{D}(\mathbf{z})$ is found as the Wigner-Weyl transform of the wave operator (Ref. [24]). Please refer to Ref. [24] for a full derivation.

A. Ray tracing

The GO equations can be solved by finding phase space trajectories, $\mathbf{z}(\boldsymbol{\tau}) = (\mathbf{x}(\boldsymbol{\tau}), \mathbf{k}(\boldsymbol{\tau}))^T$ satisfying the local dispersion relation, Eq. (4a). Such trajectories are called rays. Here, $\boldsymbol{\tau} = (\tau_1, \boldsymbol{\tau}_{\perp})^T$ where τ_1 is a longitudinal time parameter and $\boldsymbol{\tau}_{\perp} = (\tau_2, \tau_3)^T = (x_2^{(0)}, x_3^{(0)})^T$ are the perpendicular initial coordinates of the ray. Given an initial condition $\mathbf{z}(0, \boldsymbol{\tau}_{\perp}) = (\mathbf{x}_0, \mathbf{k}_0)^T$, a ray can be found from Hamilton's ray equations (Ref. [1]):

$$\partial_{\tau_1} \mathbf{x}(\tau_1) = -\partial_{\mathbf{k}}\mathcal{D}(\mathbf{x}, \mathbf{k}), \quad (6a)$$

$$\partial_{\tau_1} \mathbf{k}(\tau_1) = \partial_{\mathbf{x}}\mathcal{D}(\mathbf{x}, \mathbf{k}). \quad (6b)$$

The dispersion symbol plays the role of the Hamiltonian. In a numerical setting in multiple dimensions, we can launch a finite family of rays on a discrete $\boldsymbol{\tau}_{\perp}$ -grid all with the same initial x_1 position. Thereby, we span out a region of phase space $\mathbf{z}(\boldsymbol{\tau})$ parameterized by $\boldsymbol{\tau} \in U$, $U \subseteq \mathbb{R}^N$, where N is the number of spatial dimensions.

The mapping $\mathbf{x}(\boldsymbol{\tau}) \mapsto \mathbf{z}(\boldsymbol{\tau}) = (\mathbf{x}(\boldsymbol{\tau}), \mathbf{k}[\mathbf{x}(\boldsymbol{\tau})])^T$ from $\mathbf{x}(\boldsymbol{\tau})$ to the graph of the local wave vector is called a lift. Conversely, the inverse map from $\mathbf{z}(\boldsymbol{\tau})$ to $\mathbf{x}(\boldsymbol{\tau})$ is a projection. The set of points $\{\mathbf{z}(\boldsymbol{\tau}) \mid \boldsymbol{\tau} \in U\}$ is an N -dimensional Lagrange manifold which we call the ray manifold.

B. Field construction

Having found a ray $\mathbf{z}(\boldsymbol{\tau})$ satisfying Eq. (4a), the corresponding phase and amplitude of the eikonal field can be found by solving Eqs. (4b) and (5) with the explicit solutions:

$$\phi(\boldsymbol{\tau}) = \phi(0, \boldsymbol{\tau}_{\perp}) \sqrt{\frac{j(0, \boldsymbol{\tau}_{\perp})}{j(\boldsymbol{\tau})}}, \quad (7a)$$

$$\text{where } j(\boldsymbol{\tau}) := \det[\partial_{\boldsymbol{\tau}}\mathbf{x}(\boldsymbol{\tau})], \quad (7b)$$

$$\theta(\boldsymbol{\tau}) = \theta(0, \boldsymbol{\tau}_{\perp}) + \int_0^{\tau_1} d\tau_1 \dot{\mathbf{x}}^T(\boldsymbol{\tau}) \mathbf{k}(\boldsymbol{\tau}). \quad (8)$$

Here, $\det[\cdot]$ is the determinant of \cdot and the dot is differentiation with respect to the first coordinate τ_1 . These are the essential equations of the GO method. First, trace a set of ray phase space trajectories using Eq. (6) to obtain the ray manifold $\{(\mathbf{x}(\boldsymbol{\tau}), \mathbf{k}(\boldsymbol{\tau}))^T\}$. Then, for each ray, determine $\phi(\boldsymbol{\tau})$ from Eq. (7) and $\theta(\boldsymbol{\tau})$ from Eq. (8). If we assume that $\mathbf{x}(\boldsymbol{\tau})$ has a well-defined inverse in $\boldsymbol{\tau}(\mathbf{x})$, the final field as a function of position simply is

$$\psi(\mathbf{x}) = \psi[\boldsymbol{\tau}(\mathbf{x})] = \phi[\boldsymbol{\tau}(\mathbf{x})] e^{i\theta[\boldsymbol{\tau}(\mathbf{x})]}, \quad (9)$$

C. The caustic problem

For Eq. (9) above to be meaningful, the map $\mathbf{x}(\boldsymbol{\tau})$ needs to be bijective such that it is invertible. This is not satisfied near turning and focal points which in both cases cause rays to cross. This caustic problem is also reflected in (7), which

diverges for $j(\boldsymbol{\tau}) \rightarrow 0$. In 1D, the caustic breakdown occurs if the slope $\partial_x k(x)$ goes to infinity and therefore the local wave number function $k(x)$ does not have an explicit representation at the caustic point. In general, we shall speak of the points where $j(\boldsymbol{\tau}) = 0$ as projection singularities. Within the GO approximation, the wave field diverges exactly where the projection of the ray manifold becomes singular (Ref. [[1], p. 147]).

III. METAPLECTIC GEOMETRICAL OPTICS

MGO proposes to solve the caustic problem by continuously rotating the phase space coordinates along the ray, such that the ray manifold always has an explicit representation in the new rotated phase space coordinates. The coordinate rotations are accomplished with symplectic transforms while the corresponding transformations of the eikonal fields are accomplished with metaplectic transforms. For convenience and readability, we state in the following a few essential results on symplectic and metaplectic transforms needed to present MGO. The reader is encouraged to consult Refs. [1, 18, 25] for a more elaborate discussion on these topics.

A. Symplectic transforms

Consider linear transformations of phase space coordinates of the general form

$$\mathbf{Z} = \begin{pmatrix} \mathbf{X} \\ \mathbf{K} \end{pmatrix} := \mathbf{S} \begin{pmatrix} \mathbf{x} \\ \mathbf{k} \end{pmatrix}, \quad (10)$$

where \mathbf{S} is a $2N \times 2N$ matrix and $\mathbf{Z} = (\mathbf{X}, \mathbf{K})^T$ are the new phase space coordinates. Within MGO, we impose two constraints on the transformation matrix \mathbf{S} . First, the linear transformations must be canonical, i.e., they must preserve Hamilton's equations. It can be shown (see any of Refs. [1, 18, 25]) that this is satisfied if and only if \mathbf{S} is symplectic such that it satisfies the equation

$$\mathbf{S} \mathbf{J}_{2N} \mathbf{S}^T = \mathbf{J}_{2N}, \quad \text{where} \quad \mathbf{J}_{2N} := \begin{pmatrix} \mathbf{o}_N & \mathbf{I}_N \\ -\mathbf{I}_N & \mathbf{o}_N \end{pmatrix}. \quad (11)$$

Here \mathbf{J}_{2N} is known as the symplectic matrix and it is composed as a block matrix of the $N \times N$ zero matrix, \mathbf{o}_N , and the $N \times N$ identity matrix, \mathbf{I}_N . Furthermore, we constrain ourselves to only consider rotations, why \mathbf{S} must be orthonormal:

$$\mathbf{S}^T = \mathbf{S}^{-1}. \quad (12)$$

The orthonormality and symplecticity requirements restricts \mathbf{S} to be of the block form

$$\mathbf{S} = \begin{pmatrix} \mathbf{A} & \mathbf{B} \\ -\mathbf{B} & \mathbf{A} \end{pmatrix}, \quad (13)$$

where $\mathbf{A}, \mathbf{B} \in \mathbb{R}^{N \times N}$.

1. Generator formalism

As an alternative to (10), the symplectic transformation $\mathbf{z} \mapsto \mathbf{Z}$ can also be represented implicitly through the generator formalism. If \mathbf{B} is invertible, the first generating function is given by (Ref. [[1], Appendix E])

$$F_1(\mathbf{X}, \mathbf{x}) = -\frac{1}{2}(\mathbf{X}^T \mathbf{A} \mathbf{B}^{-1} \mathbf{X} - 2\mathbf{x}^T \mathbf{B}^{-1} \mathbf{X} + \mathbf{x} \mathbf{B}^{-1} \mathbf{A} \mathbf{x}). \quad (14)$$

$F_1(\mathbf{X}, \mathbf{x})$ is defined to generate the coordinate transformation via

$$\partial_{\mathbf{x}} F_1 = \mathbf{k}, \quad \partial_{\mathbf{X}} F_1 = -\mathbf{K}. \quad (15)$$

B. Orthosymplectic transformation for singular \mathbf{B}

References [15, 18] also treat the case where \mathbf{B} is not invertible by considering the matrix projection of \mathbf{A} onto the diagonalizing basis of \mathbf{B} . If ρ denotes the rank of \mathbf{B} and $\zeta = N - \rho$ the corank, then \mathbf{B} may be decomposed through singular value decomposition (SVD) (Refs. [18, 26]):

$$\mathbf{B} = \mathbf{L}_S \tilde{\mathbf{B}} \mathbf{R}_S^T, \quad \text{where} \quad (16)$$

$$\tilde{\mathbf{B}} = \begin{pmatrix} \Lambda_{\rho\rho} & \mathbf{o}_{\rho\zeta} \\ \mathbf{o}_{\zeta\rho} & \mathbf{o}_{\zeta\zeta} \end{pmatrix}, \quad (17)$$

$$\mathbf{L}_S^T \mathbf{L}_S = \mathbf{I}, \quad \mathbf{R}_S^T \mathbf{R}_S = \mathbf{I}, \quad (18)$$

where the columns of \mathbf{L}_S and \mathbf{R}_S are the left and right singular vectors and \mathbf{L}_S and \mathbf{R}_S are orthonormal. $\Lambda_{\rho\rho}$ is a diagonal matrix. The index $\cdot_{\mu\nu}$ denotes that the matrix is of size $\mu \times \nu$. Using the requirements of orthonormality and symplecticity it is possible to show that the matrix projection of \mathbf{A} onto the singular vectors must be block diagonal (Ref. [18]):

$$\tilde{\mathbf{A}} := \mathbf{L}_S^T \mathbf{A} \mathbf{R}_S = \begin{pmatrix} a_{\rho\rho} & \mathbf{o}_{\rho\zeta} \\ \mathbf{o}_{\zeta\rho} & a_{\zeta\zeta} \end{pmatrix}. \quad (19)$$

C. Metaplectic transforms

For each orthosymplectic transformation $\mathbf{z} \mapsto \mathbf{Z}$ of phase space coordinates, there exists a corresponding metaplectic transformation which defines how the field transforms from the old coordinate representation $\psi(\mathbf{x})$ to the new coordinate representation $\Psi(\mathbf{X})$. Assuming \mathbf{B} to be invertible, it is possible to show that the representation of the metaplectic transform of $\psi(\mathbf{x})$ in the new \mathbf{X} -space is (Ref. [18])

$$\Psi(\mathbf{X}) = \alpha \int d\mathbf{x} e^{-iF_1(\mathbf{X}, \mathbf{x})} \psi(\mathbf{x}), \quad (20)$$

where $\alpha \in \mathbb{C}$ and F_1 is the first generating function from (14). The metaplectic transform must be unitary and this determines α up to a sign. However, this leaves us with an overall sign ambiguity such that for each symplectic transformation \mathbf{S} there are two metaplectic transformations (see Ref. [[18], pp. 47–48] and Ref. [[1], p. 470] for a detailed discussion). The final integral form of the metaplectic transform of $\psi(\mathbf{x})$ is (Ref. [18])

$$\Psi(\mathbf{X}) = \frac{\pm e^{\frac{i}{2} \mathbf{x}^T \mathbf{a} \mathbf{b}^{-1} \mathbf{x}}}{(2\pi i)^{N/2} \sqrt{\det \mathbf{B}}} \int d\mathbf{x} \psi(\mathbf{x}) e^{i(\frac{1}{2} \mathbf{x} \mathbf{B}^{-1} \mathbf{A} \mathbf{x} - \mathbf{x}^T \mathbf{B}^{-1} \mathbf{X})}.$$

Here \mathbf{S} is already assumed to be of the orthosymplectic form of (13). Under the same assumption, the inverse metaplectic transform, which maps $\Psi(\mathbf{X})$ to the old representation, can be shown to be (Ref. [18])

$$\psi(\mathbf{x}) = \frac{\pm e^{-\frac{i}{2} \mathbf{x} \mathbf{B}^{-1} \mathbf{A} \mathbf{x}}}{(-2\pi i)^{N/2} \sqrt{\det \mathbf{B}}} \int d\mathbf{X} \Psi(\mathbf{X}) e^{i(-\frac{1}{2} \mathbf{X}^T \mathbf{A} \mathbf{B}^{-1} \mathbf{X} + \mathbf{x}^T \mathbf{B}^{-1} \mathbf{X})}. \quad (21)$$

Note how the metaplectic transform reduces to a Fourier transform in the special case where $\mathbf{A} = \mathbf{o}_N$ and $\mathbf{B} = \mathbf{I}_N$. In

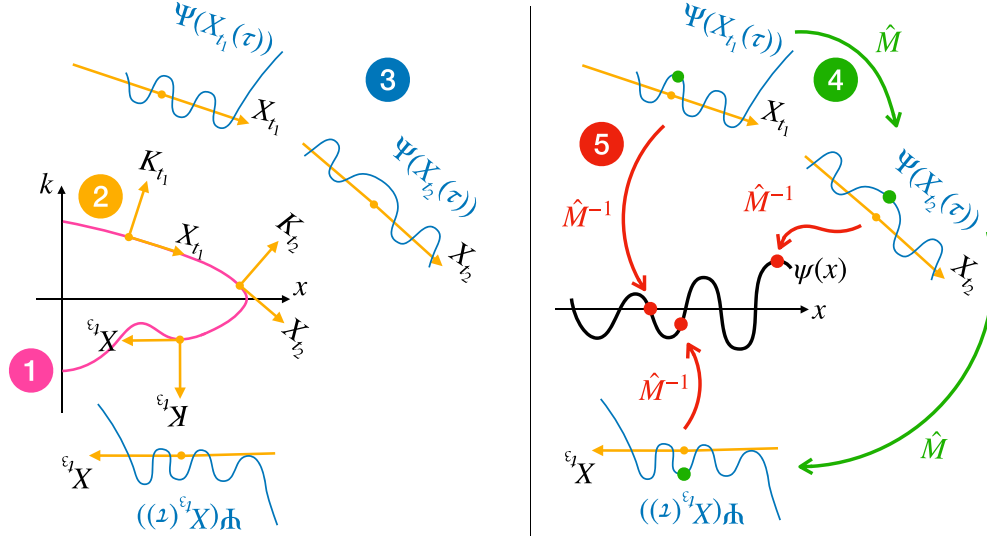


FIG. 1. Conceptual illustration of the five steps of MGO: (1) trace rays, (2) determine symplectic transformation S_t , (3) solve GO in rotated phase space, (4) link the solutions together using metaplectic transforms such that the final solution is continuous, (5) inverse metaplectic transform the fields and add up the solutions from different branches.

particular, a 1D Fourier transform is the metaplectic transform corresponding to a 90° rotation in phase space.

D. Geometrical optics in rotated phase space

Importantly, Refs. [15,18] show that under a symplectic transformation the GO Eq. (4) will carry over to the new position space. To arrive at this result, Refs. [15,18] consider an eikonal form of the metaplectically transformed field in the new position space:

$$\Psi(\mathbf{X}) = \Phi(\mathbf{X}) \exp[i\Theta(\mathbf{X})]. \quad (22)$$

References [15,18] then impose the eikonal assumption, but this time in the rotated phase space reference, i.e., $|\partial_{\mathbf{X}}\Phi| \ll |\partial_{\mathbf{X}}\Theta|$. To lowest order in the eikonal parameter, the GO equations then take the familiar form

$$\mathcal{D}[S^{-1}\mathbf{Z}(\mathbf{X})] = 0, \quad (23a)$$

$$\mathbf{V}(\mathbf{X}) \cdot \partial_{\mathbf{X}}\Phi(\mathbf{X}) + \frac{1}{2}[\partial_{\mathbf{X}} \cdot \mathbf{V}(\mathbf{X})]\Phi(\mathbf{X}) = 0, \quad (23b)$$

where $\mathbf{V}(\mathbf{X})$ is the group velocity in the new phase-space coordinates. Furthermore, Ref. [15] shows that the manifold in rotated phase space is simply obtained by transforming the original representation of the manifold:

$$\mathbf{Z}(\boldsymbol{\tau}) = \begin{pmatrix} \mathbf{X}(\boldsymbol{\tau}) \\ \mathbf{K}(\boldsymbol{\tau}) \end{pmatrix} = S\mathbf{z}(\boldsymbol{\tau}). \quad (24)$$

Therefore, in complete analogy with Eqs. (7)–(9), the new envelope and phase will have the explicit solutions in rotated phase space when away from caustics:

$$\Phi(\boldsymbol{\tau}) = \Phi(0, \boldsymbol{\tau}_\perp) \sqrt{\frac{J(0, \boldsymbol{\tau}_\perp)}{J(\boldsymbol{\tau})}}, \quad (25a)$$

$$\text{where } J(\boldsymbol{\tau}) = \det[\partial_{\boldsymbol{\tau}}\mathbf{X}(\boldsymbol{\tau})], \quad (25b)$$

$$\Theta(\boldsymbol{\tau}) = \Theta(0, \boldsymbol{\tau}_\perp) + \int_0^{\tau_1} d\tau_1 \dot{\mathbf{X}}^T(\boldsymbol{\tau})\mathbf{K}(\boldsymbol{\tau}). \quad (25c)$$

E. Review of MGO

Having presented the essentials on symplectic and metaplectic transforms, we will now present a review of the MGO method as it was developed in Refs. [14–19]. This summary is, in particular, based on Ref. [18], which the reader is encouraged to consult for a full derivation of the theory. The core idea of MGO is presented in Fig. 1. The method consists of the following five steps:

- (1) Trace a set of rays to obtain a rendering of $\mathbf{z}(\boldsymbol{\tau}) = (\mathbf{x}(\boldsymbol{\tau}), \mathbf{k}(\boldsymbol{\tau}))^T$.
- (2) For each point $\boldsymbol{\tau} = \mathbf{t}$ on the ray manifold, determine a symplectic transformation S_t which rotates the ray manifold representation into the new phase space coordinates:

$$\mathbf{Z}_t(\boldsymbol{\tau}) = (\mathbf{X}_t(\boldsymbol{\tau}), \mathbf{K}_t(\boldsymbol{\tau}))^T = S_t\mathbf{z}(\boldsymbol{\tau}).$$

The construction of S_t is given explicitly in Eqs. (27)–(30) and is designed such that the new position coordinate axes are all tangent to the ray manifold at $\boldsymbol{\tau} = \mathbf{t}$.

- (3) For each point $\boldsymbol{\tau} = \mathbf{t}$ on the ray manifold, solve the GO phase and envelope equations in the new phase space to obtain function values of $\Psi(\mathbf{X}_t)$ for all $\mathbf{X}_t(\boldsymbol{\tau})$ points.

- (4) Ensure continuity of the solution by using a near identity metaplectic transform (NIMT) to connect the initial conditions of the fields in rotated phase spaces together.

- (5) For each point $\boldsymbol{\tau} = \mathbf{t}$ on the ray manifold, inverse metaplectic transform $\Psi(\mathbf{X}_t)$ to obtain $\psi(\mathbf{x}(\mathbf{t}))$. Sum up the field contributions from all branches of the ray manifold.

The five steps are illustrated in Fig. 1. Note that there is a new transformation for each $\boldsymbol{\tau} = \mathbf{t}$ and this is reflected in the notation. For instance, $\mathbf{X}_t(\boldsymbol{\tau})$ is a function of $\boldsymbol{\tau}$ for a given fixed \mathbf{t} , while $\mathbf{X}_t(\mathbf{t})$ is this function evaluated at $\boldsymbol{\tau} = \mathbf{t}$. Finally, we denote an arbitrary coordinate set in the rotated position space as just \mathbf{X}_t and later on we shall allow \mathbf{X}_t to be complex so we can analytically continue $\Psi(\mathbf{X}_t)$. Also note how the inverse metaplectic transform maps the function $\Psi(\mathbf{X}_t)$ defined on the entire \mathbf{X}_t domain onto a single point. In the following,

we present a summary of the equations resulting from the five steps above.

Assume that the incoming wave field is defined on the boundary at position x_1 :

$$\psi_{\text{in}}(\boldsymbol{\tau}_\perp) = \phi(0, \boldsymbol{\tau}_\perp) e^{i\theta(0, \boldsymbol{\tau}_\perp)}. \quad (26)$$

Furthermore, assume that we have an initial \mathbf{z}_0 satisfying the local dispersion relation, i.e., $\mathcal{D}(\mathbf{z}_0) = 0$. The first step of the procedure is to evolve the rays using (6) to obtain $\mathbf{z}(\boldsymbol{\tau})$. Next, for all ray parameters $\boldsymbol{\tau} = \mathbf{t}$, we need to determine a symplectic rotation matrix $\mathbf{S}_\mathbf{t}$ such that the new position space coordinate axes span the tangent space of the ray manifold at $\boldsymbol{\tau} = \mathbf{t}$. This is accomplished by defining the unit vector

$$\hat{\mathbf{T}}_1(\mathbf{t}) := \partial_{\tau_1} \mathbf{z}(\mathbf{t}) / \|\partial_{\tau_1} \mathbf{z}(\mathbf{t})\|, \quad (27)$$

and then defining $\hat{\mathbf{T}}_2(\mathbf{t}), \dots, \hat{\mathbf{T}}_N(\mathbf{t})$ by Gram-Schmidt orthogonalization of the Jacobian matrix $[\partial_\tau \mathbf{z}(\boldsymbol{\tau})]^T$ (Ref. [15]). From the set of tangent vectors, one can also define a symplectically dual set of normal vectors:

$$\hat{\mathbf{N}}_j(\mathbf{t}) = -J_{2N} \hat{\mathbf{T}}_j(\mathbf{t}). \quad (28)$$

Thereby, the symplectic transformation which maps \mathbf{x} to the tangent space of the ray manifold is determined by inverting the following matrix (Ref. [15]):

$$\mathbf{S}^{-1} = \begin{pmatrix} \uparrow \hat{\mathbf{T}}_1(\mathbf{t}) & \dots & \uparrow \hat{\mathbf{T}}_N(\mathbf{t}) & \uparrow \hat{\mathbf{N}}_1(\mathbf{t}) & \dots & \uparrow \hat{\mathbf{N}}_N(\mathbf{t}) \\ \downarrow & & \downarrow & \downarrow & & \downarrow \end{pmatrix}. \quad (29)$$

As a result, the symplectic transformation matrix is now on the orthonormal form of (13):

$$\mathbf{S}_\mathbf{t} = \begin{pmatrix} \mathbf{A}_\mathbf{t} & \mathbf{B}_\mathbf{t} \\ -\mathbf{B}_\mathbf{t} & \mathbf{A}_\mathbf{t} \end{pmatrix}. \quad (30)$$

From $\mathbf{S}_\mathbf{t}$, we rotate the manifold representation using (24):

$$\mathbf{Z}_\mathbf{t}(\boldsymbol{\tau}) = \begin{pmatrix} \mathbf{X}_\mathbf{t}(\boldsymbol{\tau}) \\ \mathbf{K}_\mathbf{t}(\boldsymbol{\tau}) \end{pmatrix} := \mathbf{S}_\mathbf{t} \mathbf{z}(\boldsymbol{\tau}). \quad (31)$$

By construction, this rotation ensures that the new position coordinate axes are now tangent to the rotated manifold and therefore the manifold always has an explicit representation locally. In other words, in a neighborhood of $\boldsymbol{\tau} = \mathbf{t}$ the wave field is free from caustics and in this neighborhood it will be justified to assume the field to be of the eikonal form of (22):

$$\Psi_\mathbf{t}[\mathbf{X}_\mathbf{t}(\boldsymbol{\tau})] = \Phi_\mathbf{t}[\mathbf{X}_\mathbf{t}(\boldsymbol{\tau})] \exp(i\Theta_\mathbf{t}[\mathbf{X}_\mathbf{t}(\boldsymbol{\tau})]). \quad (32)$$

The envelope and phase field in the rotated frame is calculated using (25):

$$\Phi_\mathbf{t}[\mathbf{X}_\mathbf{t}(\boldsymbol{\tau})] = \sqrt{\frac{J_\mathbf{t}(\mathbf{t})}{J_\mathbf{t}(\boldsymbol{\tau})}}, \quad (33a)$$

$$\text{where } J_\mathbf{t}(\boldsymbol{\tau}) = \det[\partial_\tau \mathbf{X}_\mathbf{t}(\boldsymbol{\tau})], \quad (33b)$$

$$\Theta_\mathbf{t}[\mathbf{X}_\mathbf{t}(\boldsymbol{\tau})] = \int_{\tau_1}^{\tau_1} d\xi \dot{\mathbf{X}}_\mathbf{t}^T(\xi, \boldsymbol{\tau}_\perp) \mathbf{K}_\mathbf{t}(\xi, \boldsymbol{\tau}_\perp). \quad (34)$$

Note how the field in rotated phase space is renormalized such that

$$\Phi_\mathbf{t}[\mathbf{X}_\mathbf{t}(\mathbf{t})] = 1, \quad \Theta_\mathbf{t}[\mathbf{X}_\mathbf{t}(\mathbf{t})] = 0. \quad (35)$$

This renormalization choice is convenient, since it allows us to calculate $\Phi_\mathbf{t}$ and $\Theta_\mathbf{t}$ independently for each \mathbf{t} . To adjust for this renormalization and ensure continuity of the final wave field, a NIMT prefactor, $\mathcal{N}_\mathbf{t}$, will be multiplied to the final wave field.

The contribution from $\Psi_\mathbf{t}[\mathbf{X}_\mathbf{t}(\boldsymbol{\tau})]$ then needs to be brought back to the original frame. Apart from constants which we will absorb into an MGO prefactor, \mathcal{N}_τ , the inverse metaplectic transform from (21) is given by

$$\Upsilon_\mathbf{t} = \int d\boldsymbol{\epsilon} \Phi_\mathbf{t}(\boldsymbol{\epsilon}) \exp[i f_\mathbf{t}(\boldsymbol{\epsilon})], \quad (36a)$$

where

$$\Phi_\mathbf{t}(\boldsymbol{\epsilon}) := \Phi_\mathbf{t}[\mathbf{X}_\mathbf{t}(\mathbf{t}) + \boldsymbol{\epsilon}], \quad (36b)$$

$$f_\mathbf{t}(\boldsymbol{\epsilon}) := \Theta[\mathbf{X}_\mathbf{t}(\mathbf{t}) + \boldsymbol{\epsilon}] - \frac{1}{2} \boldsymbol{\epsilon}^T \mathbf{A}_\mathbf{t} \mathbf{B}_\mathbf{t}^{-1} \boldsymbol{\epsilon} - \boldsymbol{\epsilon}^T \mathbf{K}_\mathbf{t}(\mathbf{t}), \quad (36c)$$

with $\boldsymbol{\epsilon} := \mathbf{X}_\mathbf{t} - \mathbf{X}_\mathbf{t}(\mathbf{t})$. In Sec. IV C, we give details on how we calculate the integral, which in our current 1D implementation is only an integral over the real line. If, however, $\mathbf{B}_\mathbf{t}$ is singular, we must instead use the form

$$\Upsilon_\mathbf{t} = \int_{C_0} d\epsilon_\rho \Psi_\mathbf{t} \left[L_S \begin{pmatrix} \mathbf{X}_\mathbf{t}^\rho(\mathbf{t}) + \epsilon_\rho \\ a_{SS} \cdot \mathbf{x}_S(\mathbf{t}) \end{pmatrix} \right] \times \exp \left[-\frac{i}{2} \boldsymbol{\epsilon}_\rho^T a_{\rho\rho} \boldsymbol{\Lambda}_{\rho\rho}^{-1} \boldsymbol{\epsilon}_\rho - i \boldsymbol{\epsilon}_\rho^T \mathbf{K}_\mathbf{t}^\rho(\mathbf{t}) \right]. \quad (37)$$

The quantities $L_S, a_{SS}, \boldsymbol{\Lambda}_{\rho\rho}$ are defined through a SVD of $\mathbf{B}_\mathbf{t}$ as explained in Sec. III B.

The final solution to the wave field is obtained by summing up the contributions from all branches,

$$\psi(\mathbf{x}) = \sum_{i=1}^b \psi(\boldsymbol{\tau}_i(\mathbf{x})), \quad \text{where } \psi[\boldsymbol{\tau}_i(\mathbf{x})] = \mathcal{N}_{\boldsymbol{\tau}_i} \Upsilon_{\boldsymbol{\tau}_i}, \quad (38)$$

where b denotes the number of branches and the prefactor $\mathcal{N}_\mathbf{t}$ is given by

$$\mathcal{N}_\mathbf{t} = \frac{A(\boldsymbol{\tau}_\perp) \exp \left[i \int_0^{\tau_1} d\tau_1 \mathbf{k}^T(\tau_1, \boldsymbol{\tau}_\perp) \dot{\mathbf{x}}(\tau_1, \boldsymbol{\tau}_\perp) \right]}{(-2\pi i)^{\rho/2} e^{i\varphi/2} \sqrt{\det \boldsymbol{\Lambda}_{\rho\rho} \det a_{SS} \det \mathbf{R}_\mathbf{t}}}$$

Here $\varphi(\mathbf{t}) := \arg(\det(\mathbf{B}_\mathbf{t}))$. In our 1D implementation, we require that $\varphi(t)$ must be monotonically increasing for increasing t . $\mathcal{N}_\mathbf{t}$ combines the prefactor from the inverse metaplectic transform and the analytic form of the NIMT into a single analytic expression which may be evaluated independently from the integral (Ref. [18]). Note that our definition of $\mathcal{N}_\mathbf{t}$ is formulated slightly different from Ref. [18]. First, we have defined $\varphi(t)$ as the argument of $\det(\mathbf{B}_\mathbf{t})$. Since $\det(\mathbf{B}_\mathbf{t}) \in \mathbb{R}$, $\varphi(t) \in \{n\pi \mid n \in \mathbb{Z}\}$. By construction, φ must be monotonically increasing as a function of t_1 to avoid crossing branch cuts in the square root $\sqrt{\text{sign}(\det(\mathbf{B}_\mathbf{t}))} := e^{i\varphi/2}$. This is directly related to the sign ambiguity of the metaplectic transform discussed in Sec. III C. Second, as opposed to Ref. [18], we define the nonzero singular values in $\boldsymbol{\Lambda}_{\rho\rho}$ to always be positive since this is a customary convention for SVD (Ref. [[26], p. 604]). Finally, we determine the amplitude constant $A(\boldsymbol{\tau}_\perp)$ by matching the final MGO field $\psi(\mathbf{x})$ to

the true field at some x_1 coordinate, where the true field is assumed to be known in the problem. Note also that \mathbf{R}_t is the upper triangular matrix from a QR decomposition of the Jacobian matrix $\partial_\tau \mathbf{z}(\tau)$. This is not to be confused with the \mathbf{R}_S from the SVD of \mathbf{B}_t .

IV. NUMERICAL DETAILS

From this point on, we now restrict the position to be 1D, i.e., $N = 1$. This reflects the current state of the numerical implementation and the three examples on which we apply the code.

A. Obtaining the ray manifold

We obtained the ray manifold by integrating Hamilton's ray equations in (6) numerically using the initial value problem (IVP) solver from the SciPy Library (Ref. [27]) which uses a Runge-Kutta scheme. The dispersion symbol, $\mathcal{D}(\mathbf{z})$, depends on the particular physical system but its analytical form is known in examples below. To obtain the right-hand side (RHS) of (6), we used automatic differentiation with PyTorch, Ref. [28]. The IVP solver calculated the solution at discrete points on the ray manifold, and points at equidistant τ values were then interpolated with a quartic polynomial. In addition to integrating the equations forward in τ from some initial values, we also integrate backward by a smaller amount to get some ghost points on the manifold preceding our initial values. This makes the later step when we perform the inverse metaplectic transform numerically more robust.

B. Determining time derivatives, the symplectic transformation matrix and the eikonal fields

We used a finite central difference scheme with second-order precision based on the discrete known points of $\mathbf{z}(\tau)$ to calculate the Jacobian $j(\tau) = \partial_\tau \mathbf{z}(\tau)$ and its counterparts in the different rotated phase spaces $J_t(\tau) = \partial_\tau \mathbf{Z}_t(\tau)$. As an alternative, one could have used the RHS of (6) and its symplectically transformed analog. However, since we used a fine τ resolution in all examples presented below, we expect the difference between these methods to be negligible compared to the larger sources of error of the MGO method.

From $j(\tau)$ we calculated \mathbf{S}_t at all points along the ray using Eqs. (27)–(29). For each point $\tau = t$, the eikonal envelope, $\Phi_t(\tau)$, was readily calculated using $J_t(\tau)$ and (33), where we restricted the calculation to only include points on the current branch in rotated phase space. Note that we define a branch as a connected interval with a constant sign of $J_t(\tau)$. For the eikonal phase, $\Theta_t(\tau)$, in (34), we used numerical trapezoidal integration. With a fine τ resolution and well-behaved $\dot{\mathbf{x}}, \mathbf{k}$ the numerical error associated with this is expected to be negligible. Alternatively, the phase could have been calculated by integrating the τ derivative of (34) as an ordinary differential equation coupled to Hamilton's ray equations.

C. Steepest descent method for the inverse transform

From the eikonal fields, Φ_t, Θ_t in rotated phase space, we arrive at the inverse metaplectic transform integral of (36),

$$\Upsilon_t = \int_{-\infty}^{\infty} d\epsilon \Phi_t(\epsilon) e^{if_t(\epsilon)}, \quad (40)$$

where $\epsilon := X_t - X_t(t)$. Due to the oscillatory term, $e^{if_t(\epsilon)}$, the main contribution to the integral will be from the vicinity of the saddle point where $\partial_\epsilon f_t(\epsilon) = 0$. Note that by construction of $f_t(\epsilon)$ in (36c), the phase factor has a saddle point exactly at $\epsilon = 0$. Attempting to evaluate the integral along the real line by simply using the trapezoidal rule will cause erroneous numerical cancellations due to the oscillatory behavior. Instead, we have followed Refs. [17,18] which propose using the method of steepest descent and Gauss-Freud quadrature. This section explains the approach.

The steepest descent method utilizes that we may deform the integral to a new contour $\gamma(l) = \epsilon \in \mathbb{C}$ in the complex plane. This deformation of the integration path is allowed provided that the contributions to the integral as $|\epsilon| \rightarrow \infty$ vanishes and provided no singularities of the integrand $\Phi_t(\epsilon) e^{if_t(\epsilon)}$ are crossed when changing the contour path (Ref. [29], p. 158). From Eq. (33), we see that $\Phi_t(\epsilon)$ will only have singularities along the real line (at the caustics in rotated phase space). These caustics are not crossed anew by a deformation of the contour. From the definition of $f_t(\epsilon)$ in Eq. (36c), we see that $f_t(\epsilon)$ is an entire function provided the eikonal phase $\Theta_t(\epsilon)$ is entire. Thus, we can assume that a deformation of the integration path is, in general, possible. The integral is therefore

$$\Upsilon_t = \int_{\mathcal{C}_0} d\epsilon \Phi_t(\epsilon) e^{if_t(\epsilon)}. \quad (41)$$

The new integration contour \mathcal{C}_0 will be chosen as the path passing through the saddle point $\epsilon = 0$, which has the steepest descent of $|e^{if_t(\epsilon)}|$ when moving away from the saddle point. This ensures that the integral quickly converges. This is the same as finding the steepest descent of $-\text{Im}f_t(\epsilon)$. Note that $\Phi_t(\epsilon)$ is assumed to vary much more slowly than $e^{if_t(\epsilon)}$, so we only consider the behavior of $f_t(\epsilon)$ to be relevant in choosing the optimal integration contour.

1. Steepest descent directions without degeneracy

A simple analysis reveals the directions of steepest descent for a nondegenerate saddle point where $f_t''(0) \neq 0$. By construction of $f_t(\epsilon)$ in (36c), we have

$$f_t(0) = 0, \quad f_t'(0) = 0. \quad (42)$$

If $f_t''(0) \neq 0$, we may therefore approximate $f_t(\epsilon)$ in the vicinity of $\epsilon = 0$ as

$$if_t(\epsilon) \approx i \frac{1}{2} f_t''(0) \epsilon^2 = \frac{1}{2} |f_t''(0)| |\epsilon|^2 e^{i(\pi/2 + \alpha + 2\sigma)}, \quad (43a)$$

$$\text{where } \alpha := \arg f_t''(0), \quad \sigma := \arg \epsilon. \quad (43b)$$

The exponential has $\cos(\pi/2 + \alpha + 2\sigma)$ as the real part. Therefore, $|e^{if_t(\epsilon)}|$ is minimized when the cosine is -1 , i.e., in the two directions where

$$\sigma_{\pm} = -\frac{\arg f_t''(0)}{2} - \frac{\pi}{4} \pm \frac{\pi}{2}. \quad (44)$$

Since the cosine is -1 in these directions and since $f_t(0) = 0$, the real part of $f_t(\epsilon)$ will be 0 in these directions, meaning that $e^{if_t(\epsilon)}$ will be free from oscillations if evaluated along the steepest descent direction. A similar analysis for the degenerate case where $f_t''(0) = 0, f_t'''(0) \neq 0$ gives the three steepest descent directions and so forth for higher degeneracy orders.

2. Gauss-Freud quadrature

Now, assume we have found a parametrization $\gamma : \mathbb{R} \rightarrow \mathbb{C}$ of the contour such that the contour integral is

$$\Upsilon_t = \int_{-\infty}^{\infty} dl \gamma'(l) \Phi_t[\gamma(l)] e^{if_t[\gamma(l)]}. \quad (45)$$

Further, assume that the saddle point is reached at $l = 0$, i.e., $\gamma(0) = 0$. If the saddle point is degenerate, \mathcal{C}_0 may have a kink at the saddle point and it is therefore convenient to split γ into two functions:

$$\gamma(l) := \begin{cases} \gamma_-(l) & l \leq 0 \\ \gamma_+(l) & l > 0. \end{cases} \quad (46)$$

The contour integral can then be written as a single integral from 0 to ∞ :

$$\Upsilon_t = \int_0^{\infty} dl (\gamma'_-(-l) \Phi_t[\gamma_-(-l)] e^{if_t[\gamma_-(-l)]} \quad (47)$$

$$+ \gamma'_+(l) \Phi_t[\gamma_+(l)] e^{if_t[\gamma_+(l)]}). \quad (48)$$

Using Gauss-Freud quadrature, an integral of the form above can be approximated as a finite sum:

$$\int_0^{\infty} dl h(l) \approx \sum_{j=1}^n w_j \frac{h(l_j)}{\omega(l_j)}, \quad \text{where} \quad (49)$$

$$\omega(l) = e^{-l^2}. \quad (50)$$

Please refer to Refs. [17,29] for more details on the Gauss-Freud quadrature method. To reduce the error in the quadrature approximation, we need $h(l)/\omega(l)$ to be well-approximated by a $2n - 1$ degree polynomial (Ref. [29]). We shall therefore introduce a constant scaling, λ , of the parametrization, such that the integral becomes

$$\Upsilon_t = \int_0^{\infty} dl h(l), \quad \text{where} \quad h(l) := h_-(l) + h_+(l), \quad (51)$$

$$h_{\pm}(l) = \lambda (\gamma'_{\pm}(\pm \lambda l) \Phi_t[\gamma_{\pm}(\pm \lambda l)] e^{if_t[\gamma_{\pm}(\pm \lambda l)]}). \quad (52)$$

To choose λ , we note that $f_t[\gamma(l)]$ is purely imaginary and increasing, and then Taylor expand the imaginary part around $l = 0$:

$$f_t[\gamma(l)] = i \left[\left(\frac{l}{\lambda_2} \right)^2 + \left(\frac{l}{\lambda_3} \right)^3 + \dots \right], \quad (53a)$$

$$\text{where} \quad \lambda_m := \left| \frac{1}{m!} \partial_l^m \text{Im} f_t[\gamma(l)] \Big|_{l=0} \right|^{-1/m}. \quad (53b)$$

The absolute value is included to stress that we assume the m th derivative of $\text{Im} f_t[\gamma(l)]$ to be positive. We propose defining the global length scale as $\lambda = \lambda_m$, where m is the lowest positive integer for which $\lambda_m \leq \lambda_{m+1}$. With this definition, we will approximately have (in the vicinity of the saddle point)

$$f_t[\gamma(\lambda l)] \approx i l^m \quad (54)$$

and thereby

$$\frac{h_{\pm}(l)}{\omega(l)} \approx \lambda \gamma'_{\pm}(\pm \lambda l) \Phi_t[\gamma_{\pm}(\pm \lambda l)] e^{i l^{2-m}}. \quad (55)$$

The Gauss Freud quadrature is therefore appropriate if $\Phi_t(l) e^{i l^{2-m}}$ is well-approximated by a $(2n - 1)$ degree polynomial, where m is the order of degeneracy. This should

work especially well for non-degenerate saddle points, where $m = 2$.

3. Steepest descent angle update algorithm

Equation (44) is only accurate far from caustics, since the saddle point becomes degenerate at the caustic. Instead of using (44), we have therefore implemented an algorithm similar to, but slightly different from, the angle update algorithm of Ref. [17]. First, we assume that the directions of the contours are unchanged as we move away from the saddle point such that

$$\gamma(l) := \begin{cases} |l| e^{i\sigma_-} & l \leq 0 \\ |l| e^{i\sigma_+} & l > 0. \end{cases} \quad (56)$$

We start an iteration on each branch of the manifold at the τ value with a maximal value of $|j(\tau)|$. This is to ensure that we are as far from the caustics as possible such that we can use (44) as our initial values of σ_{\pm} . Then, for each point on the ray manifold we minimize $-\text{Im}[f(\epsilon)]$ on a circle of radius L and select the closest minimal loci σ_{\pm} relative to the σ_{\pm} -values found at the previous τ step. In doing so, we avoid $\sigma_+ = \sigma_-$ which would not be a valid deformation of the contour. For the radius of the circle, we choose $L = l_1 \lambda$, where l_1 is the lowest order node in the Gauss-Freud quadrature.

D. Analytic continuation to the complex plane

To evaluate the integrand along the steepest descent contour, we need to know the values of the integrand in the complex domain. This is no problem in an analytic implementation of MGO, but in a numerical treatment we only know the function values of $\Psi_t[\epsilon + X_t(t)]$ on the real domain after having calculated the phase and envelope using Eqs. (33) and (34). To solve this problem, we use barycentric rational interpolation (see Refs. [30–33]) of the numerical signal of Ψ_t, f_t . In a barycentric rational interpolation, a function $f(z)$ of a complex variable z is represented as the ratio of two partial fractions:

$$r(z) = \frac{n(z)}{d(z)} = \sum_{j=1}^m \frac{w_j f_j}{z - z_j} \Big/ \sum_{j=1}^m \frac{w_j}{z - z_j}, \quad (57)$$

where $f_j = f(z_j)$ are known sampled values of the function and w_j are weights which must be chosen. In this form, one can see that $r \rightarrow f_j$ for $z \rightarrow z_j$ why defining $r(z_j) := f_j$ for all j is meaningful such that $r(z)$ is continuous and takes the sampled values at all interpolation points. Multiplying the nominator and denominator with the node polynomial ℓ ,

$$\ell(z) = \prod_{j=1}^m (z - z_j), \quad (58)$$

shows that the barycentric representation is in fact a rational function, i.e., a quotient of two polynomials, Ref. [31]. The barycentric form is less prone to numerical overflow compared to the raw rational form, Ref. [30]. A well-known special case of barycentric interpolation is the Lagrange polynomial interpolation, which uses $w_j = \prod_{k \neq j} (z_j - z_k)^{-1}$. Rather than this choice of weights, we use the recently proposed adaptive Antoulas-Anderson (AAA) algorithm to find

the best interpolation. The algorithm is described in Ref. [31] and the Python implementation which we use is due to Refs. [32,34]. Although the algorithm generally performs well when interpolating, the precision when extrapolating an oscillatory function is generally acceptable one wavelength away from the interpolation domain, Ref. [33]. An issue in using the AAA algorithm for extrapolation is, however, that we only know the function values in a limited interval $\epsilon \in [a, b]$ along the real line. Thus, we are not guaranteed to have data in a sufficiently large radius around $\epsilon = 0$ for an interpolation to be valid. Furthermore, there may also be caustics at $\epsilon \neq 0$ in the rotated frame which can cause numerical challenges. With these considerations, we pick a maximal value M beyond which we do not extrapolate. The value is chosen based on the wave number in the rotated phase space such that

$$M = \epsilon_{\max} + \frac{\pi}{K_t(t)}, \quad (59)$$

where $\epsilon_{\max} =: \min(|a|, |b|)$. The maximal number of quadrature nodes we use is 10, but we choose the highest number of nodes, n , such that $\lambda l_n < M$, where l_n is the position of the n th quadrature node. In the worst case, where even the first quadrature node is outside the extrapolation domain, i.e., $\lambda l_1 < M$, we instead change the scaling λ to make the nodes fit inside the extrapolation domain. There is a trade-off here; more nodes improve the accuracy of the integral, but at the same time requires the barycentric rational interpolation to be valid in a larger radius in the complex domain. The choices above are an attempt to balance these considerations in an automated fashion.

E. Constructing the field

Once the inverse metaplectic transform has been applied, the branches of different signs of $j(\tau)$ must be superimposed to produce the total field. As different branches may be known at different positions and with varying resolutions, we here apply interpolation once again to evaluate the different branches in the same points. For this purpose, we use a linear interpolation scheme on the different branches of the wave field in the original frame.

V. RESULTS

Having outlined the theory of MGO and the numerical details of the implementation, we will now proceed to showcase MGO in action. The only type of caustic occurring in 1D is the fold caustic and we shall see three examples of this. First, we examine the Airy and Weber equations. Both problems are fundamental examples of caustics and have been treated analytically in the previous work by Ref. [15]. Lastly, we demonstrate the numerical implementation on a fold caustic in connection with X-B mode coupling in a hot magnetized plasma. This problem has not previously been treated using MGO, so we compare the results with PIC simulations.

A. Airy's equation

As a first example, consider Airy's equation:

$$\partial_x^2 \psi(x) - x\psi(x) = 0. \quad (60)$$

Insertion of a plane wave ansatz or alternatively taking the Wigner-Weyl transform of the wave operator gives us the local dispersion relation for Airy's equation:

$$\mathcal{D}(x, k) = -k^2 - x = 0. \quad (61)$$

A longer analytical analysis of the problem using the formulas from Sec. III gives the following fields needed for the contour integrals (Refs. [15,18]):

$$\begin{aligned} f_t(\epsilon) &= \Theta[X_t(t) + \epsilon] + k(t)\epsilon^2 - \frac{k^2(t)}{\vartheta_t}\epsilon, \\ \Theta_t[X_t(t) + \epsilon] &= \frac{8k^4(t) - \vartheta_t^4}{8k^2(t)\vartheta_t}\vartheta_t + \frac{1}{4k(t)}\epsilon^2 \\ &\quad + \frac{\vartheta_t^6 - [\vartheta_t^4 - 8k(t)\vartheta_t\epsilon]^{3/2}}{96k^3(t)}, \end{aligned} \quad (62)$$

where

$$\begin{aligned} \vartheta_t &= \sqrt{1 + 4k^2(t)}, \\ k(t) &= \sqrt{-x(t)}, \quad x(t) = -(\sqrt{x_0} - t)^2, \end{aligned}$$

and x_0 is the initial position of the traced rays. Finally, the field in the rotated frame is given by

$$\Psi_t[X_t(t) + \epsilon] = \frac{\vartheta_t}{\sqrt{4k(t)k(\tau) + 1}} e^{i\Theta_t[X_t(t) + \epsilon]}. \quad (64)$$

These analytical results will not be used to generate the numerical results but are used for benchmarking against in Fig. 3. Airy's equation has a fold caustic at $x = 0$ where the wave number k must vanish for the dispersion relation to be satisfied. In quantum mechanics, such fold caustics are encountered at turning points between the classical and nonclassical region of a potential barrier (Ref. [[35], Ch. 9]). In plasma physics, Airy's equation, for instance, arises when an O mode meets its cutoff at the critical density $n_c = \epsilon_0 m_e \omega^2 / (e^2)$. In a 1D plasma physics context, the wave field $\psi(x)$ is therefore the electric field $E(x)$. Since (60) is a second-order differential equation, it has two linearly independent basis solutions: $\text{Ai}(x)$, $\text{Bi}(x)$. Both are special cases of the modified Bessel functions which are part of the larger family of hypergeometric functions, Ref. [29]. The solution to (60) is a linear combination of these two, but since $\text{Bi}(x)$ diverges for $x \rightarrow \infty$, the solution we are interested in is the Airy function of the first kind. Up to a normalization constant, the solution therefore is

$$\psi(x) = \text{Ai}(x). \quad (65)$$

For the numerical solutions, we first trace a ray starting at $x = -8$, which propagates to $x = 0$, where it is reflected and returns to $x = -8$, at which point we automatically terminate the tracing. Using the formulas in Sec. II A along with the initial condition $\psi(-8) = \text{Ai}(-8)$, we obtain the GO solution. For the MGO solution, we trace backwards to $x \approx -13$ to provide ghost points for the calculations. Except for this fact, we use the same ray trajectory as for the GO case.

Intermediate results from the MGO algorithm for a few selected time points are shown in Fig. 2. The first time point is at the beginning, far from the caustic, the second is near the caustic, and the final time point is at the caustic. From Fig. 2(b), it is clearly visible how at all times the rotated

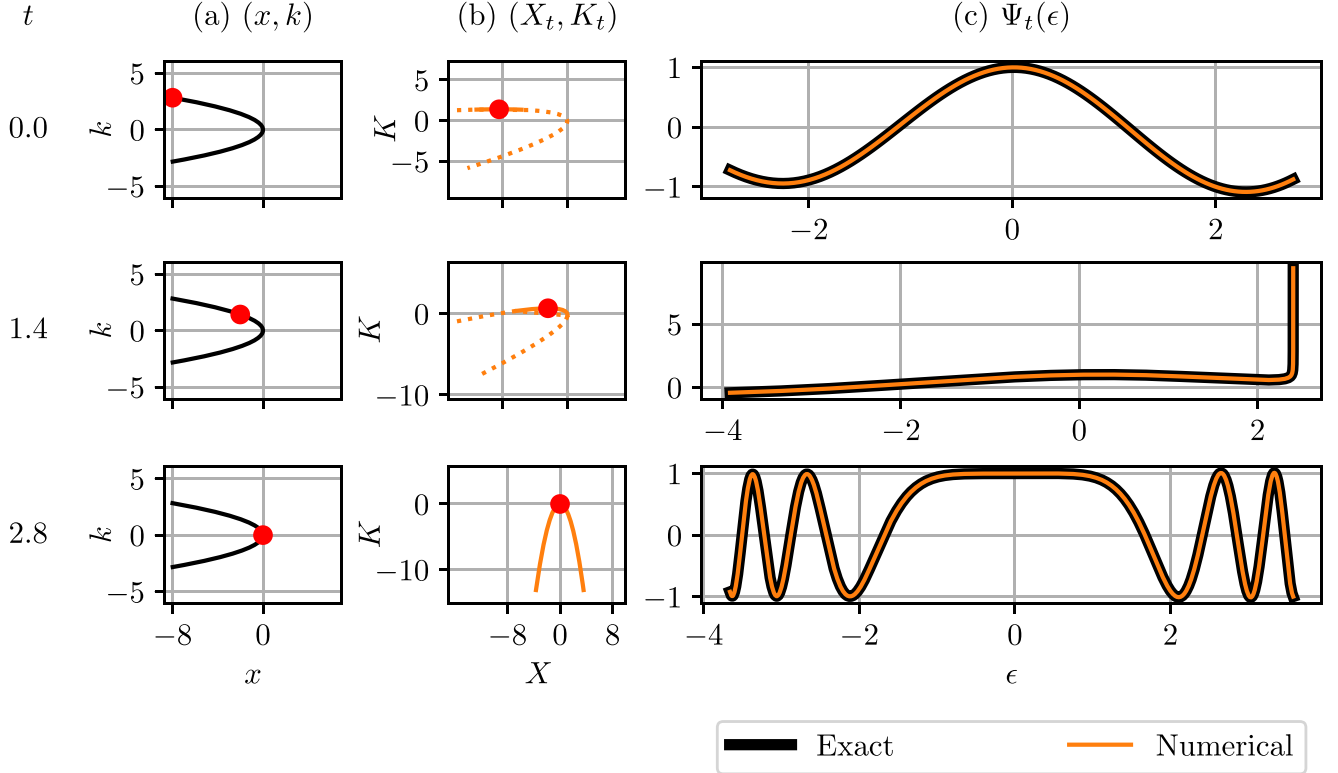


FIG. 2. Illustration of the MGO algorithm at different time points for the Airy equation example. (a) Ray manifold with red dot indicating phase space location at time t . (b) Current branch of symplectically transformed ray manifold. The solid orange line is the part of the current branch actually used for the Gauss-Freud quadrature integration. (c) Metaplectically transformed eikonal wave field $\Psi_t(\epsilon) = \Phi_t(\epsilon)e^{i\theta_t(\epsilon)}$ as a function of $\epsilon = X_t(\tau) - X_t(t)$ corresponding to symplectic transformation at time t . For (c), we have shown both the exact closed-form MGO result from (64) and the result from our numerical implementation. The core ray tracing started at $x(0) = -8$ and was automatically stopped when returning to its starting position. Besides this, a ghost point tracing was carried out to enable the calculation of the eikonal fields at the boundaries.

manifold is always tangent to the X axis at $\tau = t$. As a result, the metaplectically transformed fields plotted in Fig. 2(c) are all free from caustics in a neighborhood of $\epsilon = 0$. However, singularities may still appear further away, as is the case for $t = 1.4$. At $t = 2.8$, we meet the caustic of the original frame and the ray manifold is rotated 90° . Therefore, the metaplectically transformed eikonal field shown at the lowest plot of Fig. 2(c) is actually a Fourier transform of the Airy function. Importantly, we see excellent agreement between the exact analytical fields from (64) and our numerical fields in Fig. 2(c).

In Fig. 3, we evaluate the analytic continuation step for the phase factor $f_t(\epsilon)$ of (36c) needed in the inverse metaplectic transform. We focus in Fig. 3 on the same three time points as in Fig. 2. At all times, the barycentric rational interpolation using the AAA algorithm appears to agree very well with f_t along the real line. To investigate the analytical continuation, we show the negative imaginary part of $f_t(\epsilon)$ in Figs. 3(c) and 3(d) in the complex plane. We see no visible error between the exact result and the AAA fit in the complex plane either. At $t = 2.8$, where we meet the caustic in the original frame, we see how the degeneracy of the saddle point gives three possible steepest descent directions as explained in Sec. IV C 1. At all time points, the algorithm for finding the directions of the steepest decent contours along with the straight line assumption for the contours appear to

place the Gauss-Freud quadrature nodes close to the intended contour.

As the final steps of the MGO algorithm, we calculate the prefactor stemming from the NIMT using the initial condition. Finally, the branch contributions are interpolated and superimposed to give the final result shown in Fig. 4. In Fig. 4, we compare the three solutions along the original position axis. Of course, neither of the GO and MGO fields extends into the evanescent region $x > 0$. Far from the caustic for $x < 0$, all solutions agree very well. Near the caustic, the GO solution diverges as anticipated while the MGO solution stays close to the exact solution everywhere.

To quantify the error of the MGO solution, we show in Fig. 5 the maximal absolute deviation between the MGO solution and exact Airy function for varying parameters. Figure 5(a) shows how the error depends on the maximal degree of the barycentric rational interpolation and Fig. 5(b) shows the dependence of the error on the number of quadrature points in the Gauss-Freud quadrature. In both figures, the absolute error quickly converges to about 0.025, corresponding to a relative error of about 5%. This order of magnitude error would only result in minor corrections to most subsequent calculations. We note that the performance of this numerical implementation is comparable to the results from Ref. [17], where the exact analytical function $f_t(\epsilon)$ is known. Therefore, the error sources in our results are likely the same as

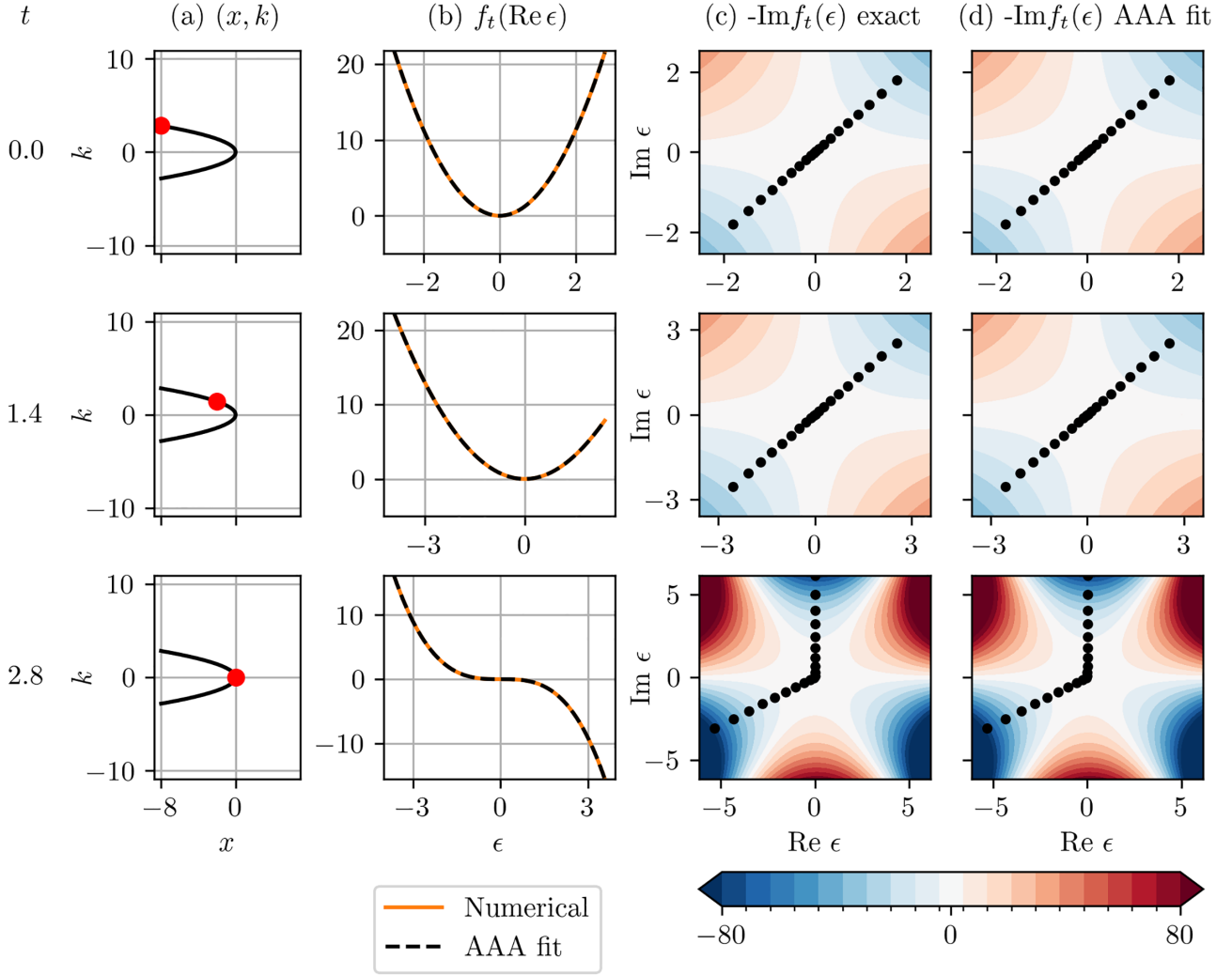


FIG. 3. Inspection of barycentric rational interpolation needed for the analytic continuation to evaluate the steepest descent integral as part of the inverse metaplectic transform step for the Airy equation example. (a) Ray manifold with red dot indicating phase-space location at time t . (b) Metaplectically transformed phase factor, f_t , as function of $\epsilon = X_t - X_t(t) \in \mathbb{R}$, (c) exact negative imaginary part of the analytically continued phase factor from Eq. (62) evaluated on $\epsilon \in \mathbb{C}$, (d) $-\text{Im}$ part of barycentric rational interpolation of f_t evaluated on $\epsilon \in \mathbb{C}$. In (b), we have included the numerical result (which in Fig. 2 was found to agree with the exact result along $\text{Re } \epsilon$), and the barycentric rational interpolation. For (c) and (d), we have also shown the Gauss quadrature node loci ($\epsilon_j = \lambda_j e^{\sigma_j}$) along the steepest descent contour used to evaluate the integral of the inverse metaplectic transform.

for the analytic MGO results previously shown in the literature. The deviations might be attributed to the limits of using Gauss-Freud quadrature near the caustic, the linear contour approximation, or, perhaps most significant, the NIMT approximation.

B. Weber's equation

As our next example, we consider Weber's equation,

$$(2E_\nu + \partial_x^2 - x^2)\psi(x) = 0, \quad (66)$$

where $E_\nu = \nu + 1/2$ and $\nu \in \mathbb{N}_0$. Weber's equation describes the quantum harmonic oscillator, with E_ν being the energy associated with the mode number ν . In a plasma physics context, this could be an O mode inside a nonmonotonic density profile, where it meets a cutoff on either side of the peak. These cutoffs are caustics and are found at $x = \pm\sqrt{2E_\nu}$. After

a Wigner-Weyl transform, the dispersion symbol is found to be (Ref. [18])

$$\mathcal{D}(x, k) = (2E_\nu - k^2 - x^2) = 0. \quad (67)$$

An exact solution can be expressed in terms of the Hermite polynomials, $H_\nu(x)$, as

$$\psi_\nu(x) = \frac{\pi^{-1/4}}{\sqrt{2^\nu \nu!}} H_\nu(x) e^{-x^2/2}. \quad (68)$$

Again, we also cite the analytical results from Refs. [15,18] of the function for the contour integral which we later compare to in Fig. 8:

$$f_t(\epsilon) = \frac{\epsilon}{2} \sqrt{2E_\nu - \epsilon^2} + E_\nu \sin^{-1} \left(\frac{\epsilon}{\sqrt{2E_\nu}} \right) - \frac{\tan(2t)}{2} \epsilon^2 - \sqrt{2E_\nu} \epsilon. \quad (69)$$

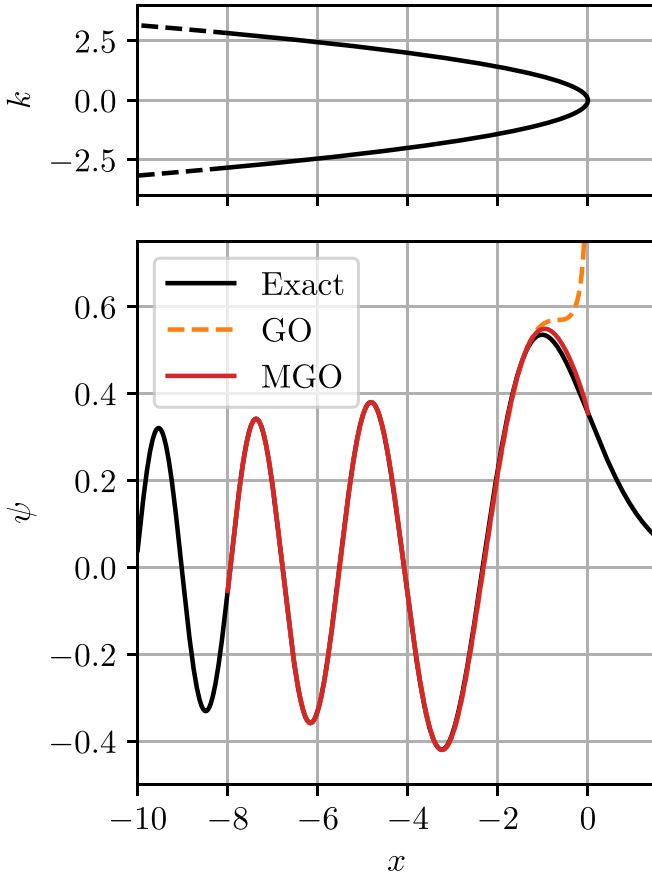


FIG. 4. Solution to Airy's equation, Eq. (60). The top plot shows the ray phase space trajectory. The solid line is the ray trace used for calculating the final field. The dashed line indicates the extra tracing carried out to get sufficient data for calculating the field at the boundaries of the trace domain. In the bottom plot, we see the resulting wave field. We have shown both the exact wave function, $\psi(x) = \text{Ai}(x)$, the GO approximation, and the solution from applying the MGO algorithm.

For the numerical solutions, we follow a very similar procedure to Airy's equation. This time, we initiate the ray tracing at $x = x_0 = -R_\nu$, since $R_\nu = \sqrt{2E_\nu}$ is the radius of the oscillation. The initial condition is chosen to match the exact solution at $x = x_0$. We use a ghost margin of 16% such that we trace 16% of the number of time points at each side of the ray trace for ghost points. We show the result of the fundamental mode in Fig. 6. Again, the GO solution diverges at the caustics, but here it only agrees well with the exact solution close to $x = 0$, in the middle between the two caustics. The MGO solution generally agrees much better with the exact solution but is visibly less accurate than for the Airy equation. Still, the solution stays within $\sim 10\%$ of the exact solution at all points. For higher mode numbers shown in Fig. 7, there is better agreement between the MGO solution and the exact solution. In phase space, the modes form closed circles of radius $\sqrt{2\nu + 1}$. The higher modes therefore have a smaller curvature, meaning that the frame is rotated slower with respect to t . When we inspect the barycentric rational AAA interpolations and the reconstructed $-\text{Im}f_i(\epsilon)$ in Fig. 8, we see that although the AAA fit is excellent inside the ϵ domain, where there is data, the contour integral uses quadrature

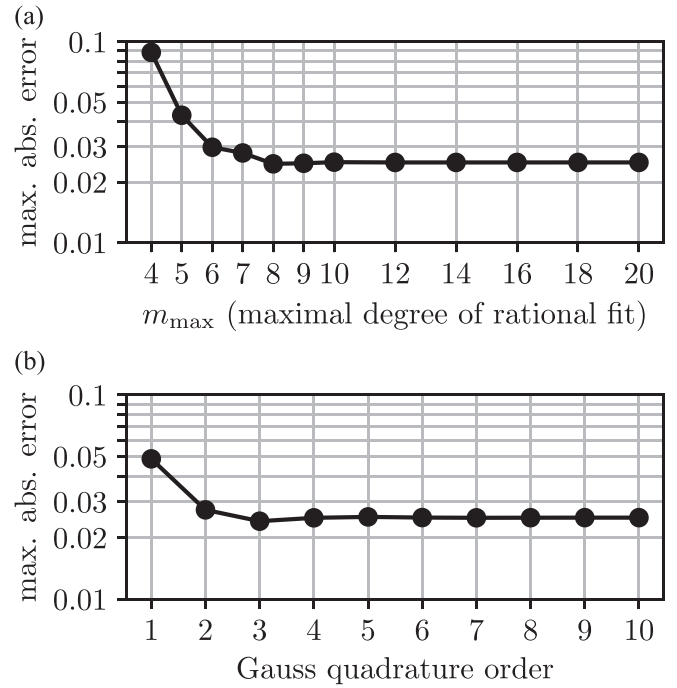


FIG. 5. Maximal absolute error (across the spatial domain) between the MGO and exact solution for the Airy problem when varying (a) the barycentric rational maximal interpolation degree and (b) the order of the Gauss-Freud quadrature. (a) used ten quadrature points and (b) used $m_{\text{max}} = 20$.

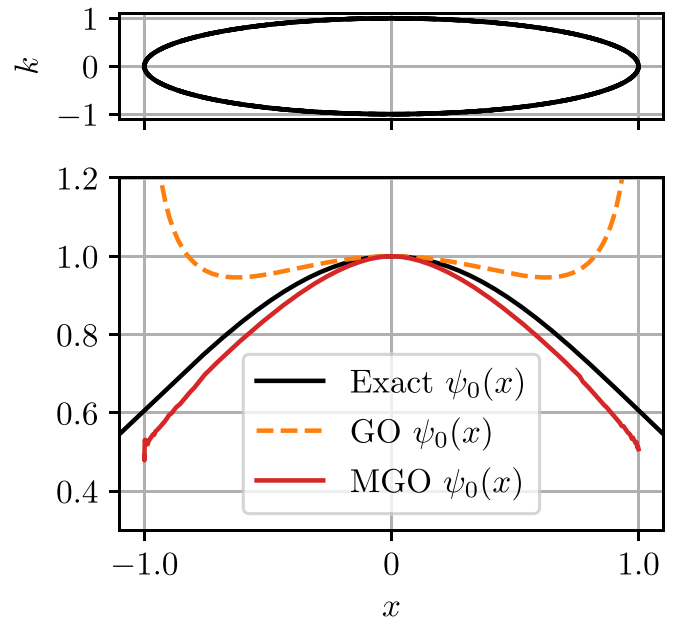


FIG. 6. Numerical solution to Weber's equation (66) for the ground state ($\nu = 0$). In the top plot, we see the ray phase-space trajectory. The ray path is seen to be periodic in phase space, and the ray tracing was automatically stopped after one cycle. However, the ray was traced a bit more than one cycle to have sufficient data on the boundaries. In the bottom, we see the reconstructed wave field in position space within the eikonal approximation of GO. For comparison, we have also included the exact wave function solution given by Eq. (68).

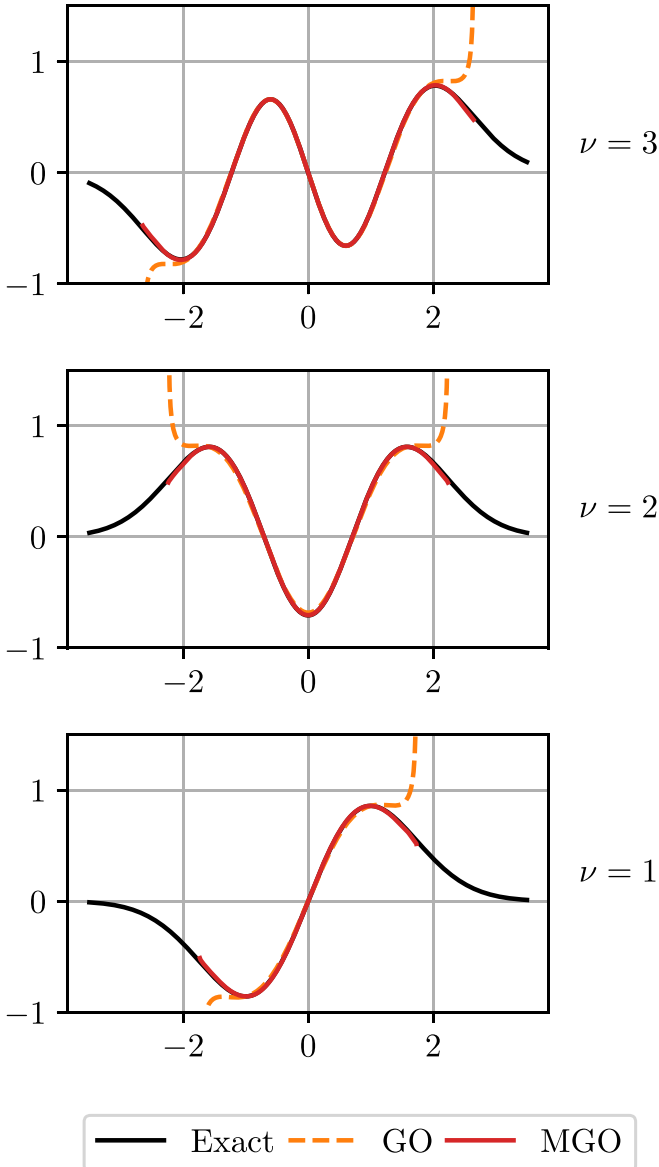


FIG. 7. Numerical solutions to Weber's equation, Eq. (68), for first three excited states $\nu = 1, 2, 3$. See caption to Fig. 6.

points which extend further away from the origin than the data points. Outside the domain, we see the occurrence of what appears to be Froissart doublets, which can be thought of as spurious pole-zero pairs very close together such that they nearly cancel, Ref. [31]. In both the purely numerical case as well as the case where $f_i(\epsilon)$ is known, the straight line contour approximation and the algorithm that determines the directions appear to mostly work well. However, some of the points furthest from the origin seem to deviate slightly from the true steepest descent contour. Still, the main contribution to the Gauss-Freud quadrature comes from the points closest to the origin where the function is reconstructed very well, and, for this reason, the final result comes close to the exact solution. We note that analytical results using the MGO method in Ref. [15] perform comparably well.

C. X-B mode coupling in ASDEX upgrade

In the final example, we apply the code to the problem of X-B coupling where the X mode couples to an EBW at the upper hybrid layer in a hot magnetized plasma. In this phenomenon, a forward propagating electromagnetic wave is coupled to a backward propagating electrostatic wave. X-B mode coupling occurs when generating EBWs for heating and current drive (Refs. [36,37]) and for wave trapping related to low threshold two-plasmon decay instabilities (Ref. [38]). The nomenclature of what is meant by X-B and the different waves vary across the literature. We refer to the forward propagating wave as the X mode, the backward propagating wave as the EBW, and the turning point as the upper hybrid layer. Unlike the cold O and X modes, the X mode and the EBW are described by the same dispersion symbol and are simply two different parts of the same ray trajectory with different physical wave characteristics. The turning point is a fold caustic and the phase space trajectory around this point is similar to that of the cutoff in Airy's equation except that the caustic occurs at nonzero k and the in- and outgoing branches describe different types of waves. This problem has not previously been treated analytically with MGO and is unlikely to ever be, as the kinetic dispersion relations for magnetized plasmas are rather complicated. In place of a comparison with analytical theory, we will make use of 1D fully kinetic PIC simulations of X-B coupling at the upper hybrid layer. We take parameters inspired by the Axially Symmetric Divertor Experiment Upgrade (ASDEX Upgrade), which is a medium-sized tokamak equipped with several gyrotrons used for electron cyclotron resonance heating and current drive as well as for collective Thomson scattering diagnostics, Refs. [39,40]. For these parameters, the upper hybrid layer of the gyrotrons is found between the fundamental and second harmonic electron cyclotron frequency.

For the PIC simulations, we use the PIC code EPOCH, Ref. [41]. It is a low power simulation that has previously been used in a study of parametric decay in ASDEX, Ref. [42], with one spatial and three velocity dimensions. It is a deuterium plasma with a linear density profile of $n_e(x) = n_i(x) = 5.4 \times 10^{19} \text{ m}^{-3} - x 2.0 \times 10^{21} \text{ mm}^{-4}$, where subscripts e and i refer to electrons and deuterons, with a uniform temperature profile of $T_e = T_i = 300 \text{ eV}$ and a magnetic field of $B = 3.35 \text{ T}$, pointing perpendicular to the x direction. The domain is $0 \text{ mm} \leq x \leq 13.5 \text{ mm}$ with 1666 grid points and 6×10^4 macroparticles per grid point, corresponding approximately to 64 gridpoints per wavelength at the upper hybrid layer. The particle boundary conditions replace lost particles at the boundaries with new thermally distributed ones. The field boundary conditions are open with a $\omega/(2\pi) = 105 \text{ GHz}$ X-mode polarized wave of intensity $I = 7 \times 10^7 \text{ W/m}^2$ at the $x = 0$ boundary. With these parameters, the upper hybrid layer is found in the vicinity of $x = 12 \text{ mm}$ and an excerpt of the longitudinal electric field can be seen in Fig. 11. An interference pattern in space can be seen in the figure and the field is seen to peak at a finite value close to $x = 12 \text{ mm}$. The field appears to have a simple harmonic time dependence on the shown timescale.

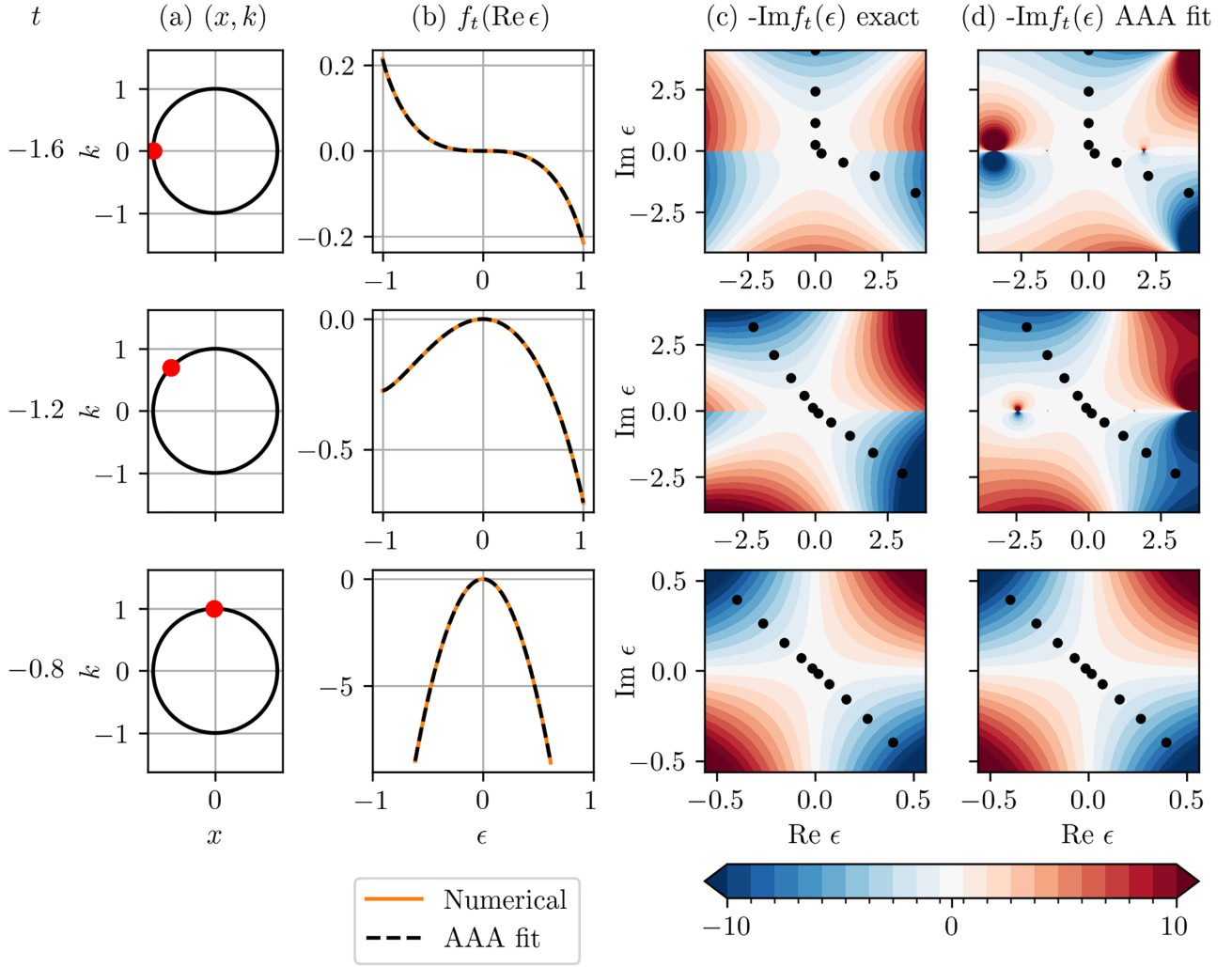


FIG. 8. Inspection of barycentric rational interpolation needed for the analytic continuation to evaluate the steepest descent integral as part of the inverse metaplectic transform step for the Weber equation example. (a) Ray manifold with red dot indicating phase space location at time t , (b) metaplectically transformed phase factor, f_t , as functions of $\epsilon = X_t - X_t(t) \in \mathbb{R}$, (c) exact $-\text{Im} f_t(\epsilon)$ from Eq. (69) evaluated on $\epsilon \in \mathbb{C}$, and (d) barycentric rational interpolation of f_t evaluated on $\epsilon \in \mathbb{C}$. In (b), we have included the numerical result and the barycentric rational interpolation. For (c) and (d), we have also shown the Gauss quadrature node loci ($\epsilon_j = \lambda l_j e^{i\theta_j}$) along the steepest descent contour used to evaluate the integral of the inverse metaplectic transform.

To model this with GO and MGO, we use the following dispersion relation (Refs. [43–45]):

$$\mathcal{D}(x, k, \omega) = K_1(x, k, \omega)k^2 - \left(\frac{\omega}{c}\right)^2 (S^2 - D^2), \quad (70)$$

$$K_1(x, k, \omega) = 1 + \frac{\omega_{\text{pe}}^2}{\omega_{\text{ce}}^2} \exp(-\lambda) \int_0^\pi d\psi \frac{\sin(\psi(\frac{\omega}{\omega_{\text{ce}}})) \sin(\psi) \exp(-\lambda \cos(\psi))}{\sin(\pi(\frac{\omega}{\omega_{\text{ce}}}))}, \quad (71)$$

where $S = 1 - \omega_{\text{pe}}^2/(\omega^2 - \omega_{\text{ce}}^2)$ and $D = \omega_{\text{ce}}\omega_{\text{pe}}^2/(\omega(\omega^2 - \omega_{\text{ce}}^2))$ are the Stix sum and difference parameters, $\lambda = k^2 v_{\text{Te}}^2/(2\omega_{\text{ce}}^2)$ is a normalized squared wave number, $\omega_{\text{ce}} = eB/m_e$ and $\omega_{\text{pe}} = \sqrt{e^2 n_e/(\epsilon_0 m_e)}$ are the electron cyclotron and plasma frequencies, and $v_{\text{Te}} = \sqrt{2T_e/m_e}$ is the electron thermal speed. Note that we are neglecting contributions from the ions because we are considering a wave in the electron

frequency range and the large mass ratio renders the ion contributions insignificant. As reported earlier in the literature, the theoretical dispersion relation does not perfectly match what is observed in EPOCH [46]. The reasons could include numerical dispersion and that nonlocal and nonlinear effects are neglected in the linear dispersion relation but not in EPOCH.

To get a better matching dispersion curve, we multiply the electron temperature by a factor of 1.28 in our GO and MGO calculations. This temperature factor was found by varying the temperature such that the absolute difference between the GO and PIC fields away from the caustic was minimized. The different ray traces corresponding to an electron temperature of 300 eV and $1.28 \times 300 \approx 385$ eV are shown in Fig. 9 on top of the spectral density from the PIC simulation. Clearly, neither of the ray traces match the numerical simulation exactly, but the curve with higher electron temperature goes through the high-intensity region in

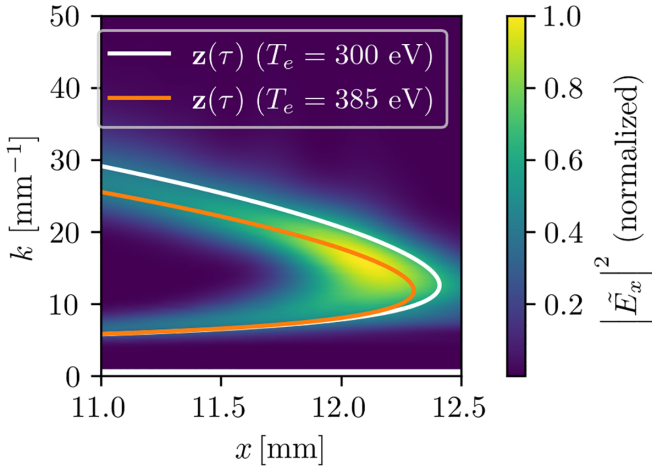


FIG. 9. Ray phase-space trajectory for X-B mode coupling plotted on top of normalized spectral density from PIC simulation. The colored spectral density plot shows the normalized norm square of the continuous wavelet transform of E_x from a PIC simulation (see Fig. 11) at a specific time ($t = 8$ ns) using a complex Morlet wavelet. Meanwhile, the white curve shows the ray trace obtained from the dispersion relation in Eq. (70) with an electron temperature of $T_e = 300$ eV. The orange curve shows the trace if instead $T_e = 385$ eV.

phase space and should therefore match better with the PIC simulation.

Similar to Airy's equation, we trace a ray starting as an X mode at $x = 0$ and end the tracing when the returning EBW reaches $x = 0$. We then reconstruct the MGO wave field and define the phase and amplitude such that the absolute difference between the MGO/GO and PIC fields is minimized across the domain $x \in [11 \text{ mm}, 11.5 \text{ mm}]$. As an alternative, one could have matched the final MGO/GO fields to the PIC simulation at a specific x location similar to the procedure of the Airy and Weber examples. However, this alternative approach would be very sensitive to the specific x location chosen since, as we shall see, we have a rapidly oscillating electric field and there is not an exact phase match between the PIC field and the MGO/GO fields.

In Fig. 10, we show the resulting incoming and outgoing and combined wave fields according to the MGO implementation. Crucially, we note that the MGO solution is finite everywhere and looks smooth except right before the turning point on the right side, where the curve becomes a little noisy. We attribute this noise to the interpolation based on the AAA algorithm in combination with the straight contour approximation which leads the contours close to spurious poles of the AAA extrapolation.

Finally, we compare the amplitude of the complex envelope function of both the GO and MGO solutions with that of the PIC simulations. Since the fields are real-valued in the PIC simulations, we determine the envelope as the maximum in the time interval $6.5 \text{ ns} < t < 12 \text{ ns}$ at each grid point inside the domain. No clear transients occur near the upper hybrid layer in this period. The resulting comparison is shown in Fig. 12. All solutions agree well on shape and magnitude with some minor deviations, except for the GO solution which diverges at the upper hybrid layer. It is worth noting that the

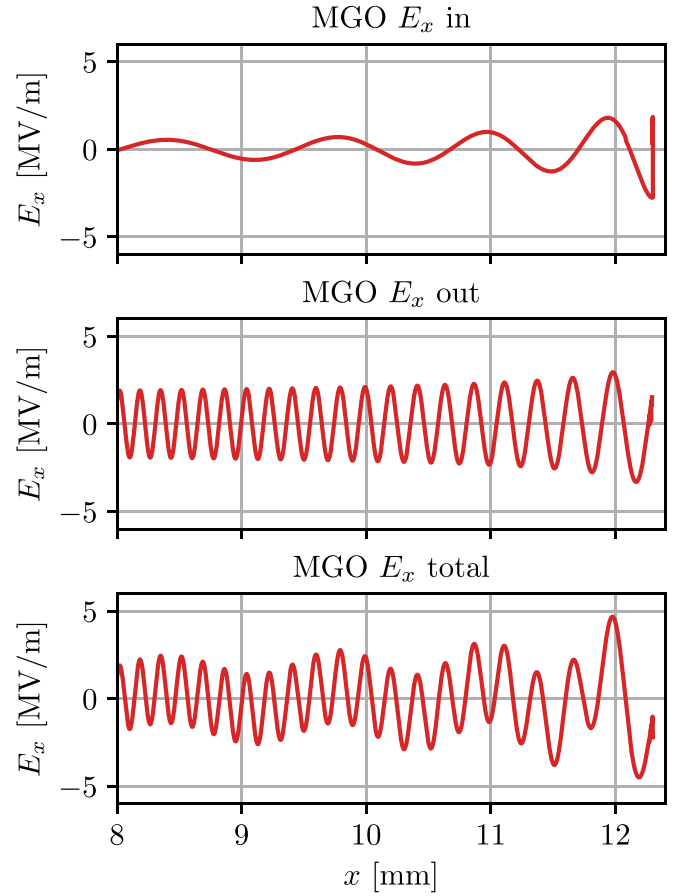


FIG. 10. Plots of the ingoing (top plot), outgoing (center plot), and combined (bottom plot) field obtained from MGO for the case of X-B mode coupling with $T_e = 385$ eV.

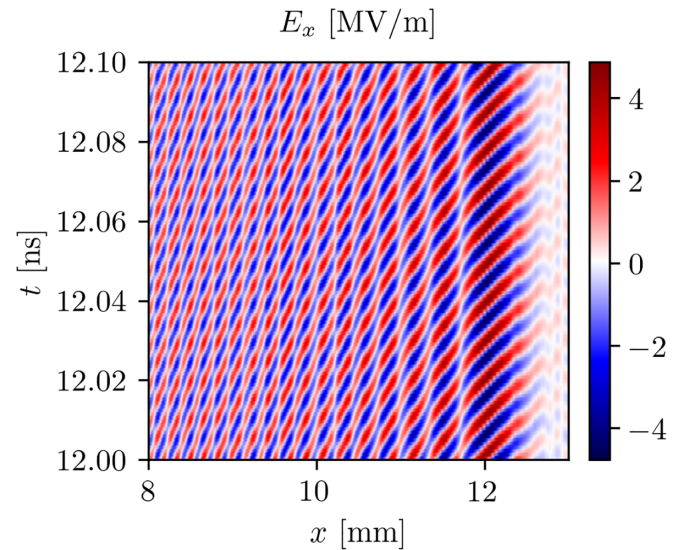


FIG. 11. Longitudinal electric field, E_x , in 1D PIC simulations of X-B mode coupling in ASDEX. An X-mode wave is excited at $x = 0$ mm and propagates to the upper hybrid layer near $x = 12$ mm where it couples to a backward propagating electron Bernstein wave. At the shown time, the returning electron Bernstein wave has made it back to the left boundary of the figure and an interference pattern can be seen.

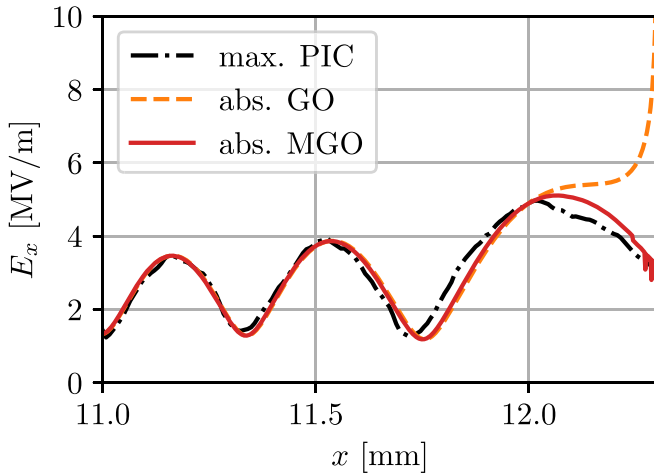


FIG. 12. A comparison of the envelope of the longitudinal electric wave field for X-B mode coupling. The absolute value of the GO/MGO fields (with $T_e = 385$ eV) are compared to the maximum of the PIC result (the PIC field is maximized over a time window of about 5 ns). The amplitude of the GO and MGO solutions were set by minimizing the absolute difference between the absolute MGO field and the maximum PIC field over the interval $x \in [11 \text{ mm}, 11.5 \text{ mm}]$.

PIC simulations model many more effects than the simple linear dispersion relation is capturing. As mentioned earlier, nonlocal and nonlinear effects are neglected even though the upper hybrid layer is often associated with nonlinear effects due, in part, to the caustic. Furthermore, although both the X-mode and electron Bernstein wave become approximately electrostatic near the upper hybrid layer, the X-B mode coupling is not truly a scalar wave problem. Still, our numerical implementation of MGO is capable of capturing the features of the PIC wave field, provided that the dispersion manifold can be determined sufficiently well.

VI. CONCLUSION AND DISCUSSION

We have presented an unsupervised numerical implementation of MGO, relying only on a 1D discrete phase space trajectory produced by a ray tracer. The code needs no additional information to the ray tracer and reconstructs the wave field with good agreement, and importantly without singularities, for the benchmarking examples of Airy's and Weber's equation. The numerical solutions display minor deviations near the caustics with a relative error within 10% in the worst case example in Weber's equation. This discrepancy may be

attributed to the numerical integration method used to evaluate the inverse metaplectic transform or to an approximation of the NIMT. The contour integrals are performed using Gauss-Freud quadrature and a barycentric rational function fit, which reconstructs the target functions with great precision and does a decent job extrapolating to the complex domain. A problem in the current implementation is that the barycentric rational interpolation suffers from Froissart doublets. An approach to remove these doublets is proposed in Ref. [31], but not yet implemented in the numerical implementation presented here. Though there is room for optimization, our numerical implementation reconstructs the wave field in seconds to a few minutes on a modern laptop (MacBook Pro 2019), depending on the resolution needed for the problem (about 30 s for Airy's equation with 700 ray tracing points and 1.5 min for the X-B example with 2500 ray tracing points). The numerical implementation is fully automated and the implementation can, in principle, be extended to more spatial dimensions in future work. However, it remains an unresolved problem to generalize the steepest-descent methods used in 1D in this paper to multidimensional integrals. Importantly, the MGO algorithm is agnostic to the type of linear wave equation, though the current formulation of MGO is reserved to time-invariant scalar waves.

When applied to the problem of X-B mode coupling in a magnetized fusion plasma, the numerical implementation of MGO is capable of achieving good agreement with PIC simulations, with similar or better performance than GO and, crucially, without the divergent behavior at the caustic. This opens up applications in reduced modeling of phenomena which depend nonlinearly on the electric field intensity such as three-wave interactions and stochastic heating.

ACKNOWLEDGMENTS

We thank Dr. N. Lopez for fruitful discussions. This work has been carried out within the framework of the EUROfusion Consortium, funded by the European Union via the Euratom Research and Training Programme (Grant Agreement No. 101052200—EUROfusion). The work presented here is supported by the Carlsberg Foundation, Grant No. CF23-0181, and the Novo Nordisk Foundation, No. NNF22OC0076017.

Views and opinions expressed are those of the author(s) only and do not necessarily reflect those of the European Union or the European Commission. Neither the European Union nor the European Commission can be held responsible for them.

- [1] E. R. Tracy, A. J. Brizard, A. S. Richardson, and A. N. Kaufman, *Ray Tracing and Beyond: Phase Space Methods in Plasma Wave Theory* (Cambridge University Press, Cambridge, England, 2012).
- [2] D. B. Batchelor, R. C. Goldfinger, and H. Weitzner, *IEEE Trans. Plasma Sci.* **8**, 78 (1980).
- [3] A. J. H. Donné, *Rev. Sci. Instrum.* **66**, 3407 (1995).
- [4] S. K. Nielsen, H. Bindslev, L. Porte, J. A. Hoekzema, S. B. Korsholm, F. Leipold, F. Meo, P. K. Michelsen, S. Michelsen,

- J. W. Oosterbeek, E. L. Tsakadze, G. Van Wassenhove, E. Westerhof, and P. Woskov, *Phys. Rev. E* **77**, 016407 (2008).
- [5] R. Prater, D. Farina, Y. Gribov, R. Harvey, A. Ram, Y.-R. Lin-Liu, E. Poli, A. Smirnov, F. Volpe, E. Westerhof, A. Zvonkov, and I. S. S. O. T. Group, *Nucl. Fusion* **48**, 035006 (2008).
- [6] K. Nagasaki, A. Isayama, N. Hayashi, T. Ozeki, M. Takechi, N. Oyama, S. Ide, S. Yamamoto, and the JT-60 Team, *Nucl. Fusion* **45**, 1608 (2005).

- [7] J. Preinhaelter and V. Kopecký, *J. Plasma Phys.* **10**, 1 (1973).
- [8] A. K. Ram and S. D. Schultz, *Phys. Plasmas* **7**, 4084 (2000).
- [9] R. B. White and F. F. Chen, *Plasma Phys.* **16**, 565 (1974).
- [10] C. F. F. Karney and A. Bers, *Phys. Rev. Lett.* **39**, 550 (1977).
- [11] M. Porkolab and R. P. H. Chang, *Rev. Mod. Phys.* **50**, 745 (1978).
- [12] P. Aleynikov and N. B. Marushchenko, *Comput. Phys. Commun.* **241**, 40 (2019).
- [13] A. Köhn-Seemann, B. E. Eliasson, S. J. Freethy, L. A. Holland, and R. G. Vann, *EPJ Web Conf.* **277**, 01010 (2023).
- [14] N. A. Lopez and I. Y. Dodin, *J. Opt. Soc. Am. A* **36**, 1846 (2019).
- [15] N. A. Lopez and I. Y. Dodin, *New J. Phys.* **22**, 083078 (2020).
- [16] N. A. Lopez and I. Y. Dodin, *J. Opt. Soc. Am. A* **38**, 634 (2021).
- [17] S. M. Donnelly, N. A. Lopez, and I. Y. Dodin, *Phys. Rev. E* **104**, 025304 (2021).
- [18] N. A. Lopez, *Metaplectic geometrical optics*, Ph.D. thesis, Princeton University, 2022.
- [19] N. A. Lopez and I. Y. Dodin, *Phys. Plasmas* **29**, 052111 (2022).
- [20] V. Maslov and M. Fedoriuk, *Semi-Classical Approximation in Quantum Mechanics*, Mathematical Physics and Applied Mathematics (D. Reidel Publishing Co., Dordrecht, Holland, 1981), Vol. 7.
- [21] J. B. Keller, *SIAM Rev.* **27**, 485 (1985).
- [22] R. Højlund, GitHub Repository: plasma-ray-tracer (2024), <https://github.com/runehoejlund/plasma-ray-tracer.git>.
- [23] E. Mazzucato, *Electromagnetic Waves for Thermonuclear Fusion Research* (World Scientific Publishing Co., Singapore, 2014), pp. 1–204.
- [24] I. Y. Dodin, D. E. Ruiz, K. Yanagihara, Y. Zhou, and S. Kubo, *Phys. Plasmas* **26**, 072110 (2019).
- [25] H. Goldstein, C. Poole, and J. Safko, *Classical Mechanics*, 3rd ed. (Pearson/Addison-Wesley, Upper Saddle River, NJ, 2002).
- [26] J. Nocedal and S. J. Wright, *Numerical Optimization* (Springer, New York, USA, 2006).
- [27] The SciPy Community, SciPy IVP Solver Documentation (2024).
- [28] A. Paszke, S. Gross, F. Massa, A. Lerer, J. Bradbury, G. Chanan, T. Killeen, Z. Lin, N. Gimelshein, L. Antiga, A. Desmaison, A. Köpf, E. Yang, Z. DeVito, M. Raison, A. Tejani, S. Chilamkurthy, B. Steiner, L. Fang, J. Bai, and S. Chintala, [arXiv:1912.01703](https://arxiv.org/abs/1912.01703).
- [29] A. Gil, J. Segura, and N. M. Temme, *Numerical Methods for Special Functions* (Society for Industrial and Applied Mathematics, Philadelphia, USA, 2007).
- [30] J.-P. Berrut and G. Klein, *J. Comput. Appl. Math.* **259**, 95 (2014).
- [31] Y. Nakatsukasa, O. Sète, and L. N. Trefethen, *SIAM J. Sci. Comput.* **40**, A1494 (2018).
- [32] C. Hofreither, *Numer. Algor.* **88**, 365 (2021).
- [33] L. N. Trefethen, *Jpn. J. Ind. Appl. Math.* **40**, 1587 (2023).
- [34] Hofreither, Clemens, GitHub Repository: baryrat (2024), <https://github.com/c-f-h/baryrat>.
- [35] D. J. Griffiths, *Introduction to Quantum Mechanics*, 3rd ed. (Cambridge University Press, Cambridge, United Kingdom, 2018).
- [36] H. P. Laqua, V. Erckmann, H. J. Hartfuß, and H. Laqua (W7-AS Team ECRH Group), *Phys. Rev. Lett.* **78**, 3467 (1997).
- [37] X. Guo, R. Ashida, Y. Noguchi, R. Kajita, H. Tanaka, M. Uchida, and T. Maekawa, *Plasma Phys. Controlled Fusion* **64**, 035008 (2022).
- [38] A. Clod, M. G. Senstius, A. H. Nielsen, R. Ragona, A. S. Thrysoe, U. Kumar, S. Coda, and S. K. Nielsen (TCV team), *Phys. Rev. Lett.* **132**, 135101 (2024).
- [39] O. Kudlacek, P. David, I. Gomez, A. Gräter, B. Sieglin, W. Treutterer, M. Weiland, T. Zehetbauer, M. V. Berkel, M. Bernert, T. Bosman, F. Felici, L. Giannone, J. Illerhaus, D. Kropackova, P. Lang, M. Maraschek, B. Ploekl, M. Reich, and A. V. Kubincova, *Nucl. Fusion* **64**, 056012 (2024).
- [40] S. K. Hansen, S. K. Nielsen, J. Stober, J. Rasmussen, M. Salewski, and M. Stejner, *Phys. Plasmas* **26**, 062102 (2019).
- [41] T. D. Arber, K. Bennett, C. S. Brady, A. Lawrence-Douglas, M. G. Ramsay, N. J. Sircombe, P. Gillies, R. G. Evans, H. Schmitz, A. R. Bell, and C. P. Ridgers, *Plasma Phys. Controlled Fusion* **57**, 113001 (2015).
- [42] M. G. Senstius, S. K. Nielsen, R. G. Vann, and S. K. Hansen, *Plasma Phys. Controlled Fusion* **62**, 025010 (2020).
- [43] M. G. Senstius, S. J. Freethy, and S. K. Nielsen, *Phys. Plasmas* **31**, 032308 (2024).
- [44] F. W. Crawford and J. A. Tataronis, *J. Appl. Phys.* **36**, 2930 (1965).
- [45] S. K. Hansen, *Parametric decay instabilities in the electron cyclotron resonance heating beams at ASDEX Upgrade*, Ph.D. thesis, Technical University of Denmark, 2019.
- [46] M. G. Senstius, S. K. Nielsen, and R. G. L. Vann, *Plasma Phys. Controlled Fusion* **63**, 065018 (2021).